UNIVERSITY OF CALIFORNIA

Los Angeles

High Frequency Guided Wave Propagation in Layered Media

A dissertation submitted in partial satisfaction
of the requirements for the degree
Doctor of Philosophy in Mechanical Engineering

by

Lifu Wang

2023

ABSTRACT OF THE DISSERTATION

High Frequency Guided Wave Propagation

in Layered Media

by

Lifu Wang

Doctor of Philosophy in Mechanical Engineering

University of California, Los Angeles, 2023

Professor Ajit K. Mal, Chair

Honeycomb sandwich structures (HSS), due to their high strength/stiffness to density ratio, are widely used in aerospace industry. Efficient and reliable techniques are required to detect damages in HSS. While conventional damage detection methods cannot meet the requirements, ultrasonic guided waves, due to their long propagating range and sensitivity to different types of defects, have the potential to significantly improve the state-of-the art in the NDE of HSS. However, the literature on ultrasound propagation in HSS is rather sparse, especially on the detailed characteristics of the waves and their interaction with realistic defects in HSS components. When the defect is smaller, excitation signal with higher frequency is required. However, there is no published research on this subject.

The major objective of this research is to study high frequency wave propagation in HSS with or without the presence of defects. A numerical searcher is developed to solve the dispersion equations in HSS under very high frequency excitations. With this tool, solutions for high frequency Lamb waves in isotropic media are obtained and compared with numerical simulations. To obtain the solution in layered media, the global matrix method (GMM) is used

and solutions for force responses are obtained by the residue theorem. However, the conventional method has singularity issues causing numerical instability in certain frequencies. A new formulation of the method is developed to solve the problem. The HSS is later homogenized to a three-layered medium and the dispersion curves for this model is studied with changes in the core material properties. At the end, the conventional damping model for Lamb waves is validated through the method and the corresponding damping coefficients are obtained experimentally.

An experiment is performed to obtain the signal features when disbond damages are introduced in the HSS. The characteristics of the waves incident from different angles are studied to identify the most favorable incident angle for defects detection Based on this study, a new damage index is extracted from the signals and is applied to improve the quality of the damage detection images. Finally, an experiment is performed about the feasibility of using non-contact transducers to detect damages in HSS.

The dissertation of Lifu Wang is approved.

Vinay Goyal

Robert M'Closkey

Woody Ju

Khalid Jawed

Christoph Schaal

Ajit Mal, Committee Chair

University of California, Los Angeles

2023

TABLE OF CONTENTS

LIST OF FIGURES

ACKNOWLEDGEMENTS

I appreciate all people who has helped me a lot in finishing this work. It would be impossible without your helps.

Firstly, I am thankful to my advisor, Professor Mal, for his kindness and support. When I was struggling whether I should pursue a doctorial degree, it was him who encouraged me and at the same time provided me with economic support. His knowledge and experience affect me in many ways, pushing me to study and become a mature individual. I am lucky to have him as my advisor and I will never forget him and the life I work with him in UCLA.

I would like to thank the committee members, Professor Goyal, Ju, Khalid, M'Closkey and Schaal, for all the advices and guidance. I extremely appreciate Professor Schaal for all the advice and cooperation during these years. He is such an knowledgeable person and I learn from him every time we have a conversation. Professor Goyal also plays an important role in my life. It was a pleasure to be his TA for the FEM class. I have learnt a lot from him. I also want to express my thank to Dr. Amiya Chatterjee. It was a pleasure work as his TA for many classes.

I do not have enough words to express my thanks to my dear friends, Steffen Tai and Leonardo Araque. Their kindness makes me feel like I am at home even when I am studying abroad and do not have any family nearby. I learnt a lot from them. I will never reach this step without the help of you two. I also want to express my thanks to Professor Fei Gao, and Yichi Zhang. They have played very important roles in my doctorial life.

I do not know how to express my thanks to my mother and father, Xia Lin and Mingjun Wang, who have raised, educated, encouraged and supported me until this moment. I am forever in debt to you. After these years, do I become the person you are proud of?

Lastly, appreciation to my girl, Luna, who has been standing by my side all the time, comforting me whenever I am exhausted and sharing the painful and joyful moments with me. Forever love.

VITA

2012-2016	B.S. in Theoretical and Applied Mechanics, Sun Yat-sen University, Guangzhou China
2014-2016	B.S. in Mechanical Engineering, IUPUI, Indianapolis
2016-2017	M.S. in Mechanical Engineering, University of California, Los Angeles
2019	Ph.D. Advanced to Candidacy

PUBLICATIONS

Articles in Journals

1. Wang, L., Gao, F., Zhang, Y., Araque, L., Patel, B., Tai, S., and Mal, A., "An Improved Damage Index for Non-destructive Evaluation of a Disbond in Honeycomb Sandwich Structure Using Guided Waves," Journal of Nondestructive Evaluation, Diagnostics and Prognostics of Engineering Systems, Vol. 3, 2020, pp. 1–14.
2. Araque, L., Wang, L., Mal, A., and Schaal, C., "Advanced Fuzzy Arithmetic for Material Characterization of Composites Using Guided Ultrasonic Waves," Mechanical Systems and Signal Processing, Vol. 171, 2022
3. Gao, F., Hua, J., Wang, L., Zeng, L., and Lin, J., "Local Wavenumber Method for Delamination Characterization in Composites with Sparse Representation of Lamb Waves," IEEE Transactions of Ultrasonics, Ferroelectrics, and Frequency Control, 2020, pp. 1305-1313
4. Gao, F., Wang, L., Hua, J., Lin, J., and Mal, A., "Application of Lamb Wave and its Coda Waves to Disbond Detection in an Aeronautical Honeycomb Composite Sandwich," Mechanical Systems and Signal Processing, Vol.146, 2021,
5. Tai, S., Kotobuki, F., Wang, L., Mal, A., "Modeling Ultrasonic Elastic Waves in Fiber-Metal Laminate Structures in Presence of Source and Defects," Journal of Nondestructive Evaluation Diagnostics and Prognostics of Engineering System, Vol.3 2020 pp. 1-42

Conference Papers

1. Wang, Lifu & Araque, Leonardo & Tai, Steffen & Mal, Ajit & Schaal, Christoph. (2019). Feasibility Analysis of Various Sensing Methods for Nondestructive Testing of Composites. 10.12783/shm2019/32115.
2. Wang, Lifu & Araque, Leonardo & Tai, Steffen & Schaal, Christoph & Mal, Ajit (2021). Features of Guided Waves Propagating in a Honeycomb Sandwich Structure. QNDE, 10.1115/QNDE2021-75053
3. Araque, Leonardo & Wang, Lifu & Mal, Ajit & Schaal, Christoph. (2021). Inverse fuzzy arithmetic for material characterization of composites using guided waves. 26. 10.1117/12.2583947.
4. Araque, Leonardo & Wang, Lifu & Mal, Ajit & Samaratunga, Dulip & Sagrillo, Christopher & Rome, Jacob. (2021). Guided ultrasonic wave-based technique for assessment of composite structures with prior damage. 10.2514/6.2021-1081.
5. Araque, Leonardo & Wang, Lifu & Tai, Steffen & Mal, Ajit & Schaal, Christoph. (2020). Uncertainty characterization of guided ultrasonic wave properties in composite materials. 21. 10.1117/12.2558853.
6. Tai, Steffen & Wang, Lifu & Araque, Leonardo & Mal, Ajit & Schaal, Christoph. (2019). Effects of Homogenization and Quasi-Isotropy Assumptions on Guided Wave-Based Nondestructive Testing Methods. 10.12783/shm2019/32197.

Chapter 1 Introduction

1.1 Motivation

1.1.1 Background of nondestructive evaluation (NDE) based on guided waves

Evaluation of material degradation without destroying the structure has been studied for almost a century and many tools have been implemented for NDE of critical structural components. Ultrasound, due to its low cost, safety and high efficiency, is widely used for NDE of a variety of structures. Conventional methods for NDE using ultrasound include pulse echo and pitch catch arrangements of single or multiple transducers that can generate bulk waves in the test article. It is well known that on guided Lamb type waves can be an effective tool in NDE and SHM of layered structures due to their long range of propagation and high sensitivity to defects in their paths [1-4]. However, in contrast to bulk waves, Lamb waves are dispersive and contains multiple modes that can be used to detect defects of different sizes and depths but it makes the data interpretation and defects characterization more challenging. Therefore, studying how guided waves propagate in varies media and how they interact with different defects are important so that we can differentiate amongst different types of defects.

1.1.2 Thick plate response

Lamb waves that commonly applied in NDE is in a frequency range with frequency-thickness product from 50kHz · mm to 3000 kHz · mm. For example, Yashiro et al. in his paper explored the NDT method based on Lamb wave with 300kHz central frequency excitation in a 3mm composite plate [1]. In another paper, Michal et al studied the response of their transducer at a working frequency from 100kHz to 500kHz in a 4mm thick plate [2]. Gao and his coauthors, he

proposed an amplitude modified method based on Lamb wave detection with a working frequency below 1MHz in a 2mm thick composite plate [3]. The selection of frequency is usually based on the sensor of excitation. However, in order to achieve better resolution in sensing, more and more research becomes interested in high frequency excitation. For example, Greve et al studied the excitation of 15MHz · mm in a plate [4]. Few research is done on Lamb waves in plate with a thickness more than 50MHz · mm. To fill the gap, more research needs to be done to clarify the responses of the Lamb waves at higher values of the frequency×thickness.

1.1.3 Honeycomb sandwich structure

Honeycomb sandwich structures refer to the composite structures with large in-plane stiffness solid skin material such as carbon-fiber composite, and a low-density cellular core with shear rigidity. They combine the advantages of high level of bending stiffness and low density, and therefore, widely used in aerospace industry [5]. The honeycomb sandwich structures usually have a layer of in-plane stiff material, following with an adhesive layer. The honeycomb sandwich core is bonded next to the adhesive layer. The core is vented to avoid pressure change inside the honeycomb sandwich cores.

Amount all the failures, disbond between the face sheet and the core is the most commonly seem defect, and sometimes is invisible from the surface of the panel.

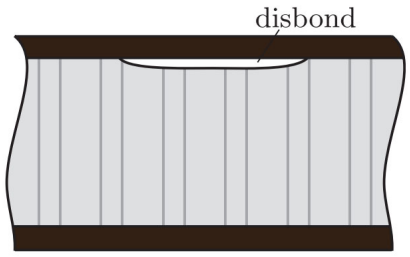

Figure 1-1 Example of a Disbond in a Honeycomb Sandwich Panel [6]

Honeycomb sandwich structures are important in the aerospace industry that many accidences are caused by material failure of the honeycomb sandwich structures. For example, in 2002, an F-15E crashed because of the structural failure of the honeycomb material in a vertical stabilizer leading edge [7]. Applying NDE on Honeycomb Sandwich Structures is very important for defect inspection. The smaller the defect that can be detected, the more robust the design can be.

1.1.4 Wave propagation in a honeycomb sandwich structure

Some common techniques for NDE in the honeycomb sandwich structures include ultrasonic C scan [8], thermography inspection and x-ray inspection [9]. Other inspection method for metallic honeycomb structures may includes the use of eddy currents [10]. Using guided wave for NDE in honeycomb sandwich structures is not new. The wave propagation inside the honeycomb sandwich structures has been studied by a number of researchers. And yet, there are no conclusive results as to the waves propagate in the honeycomb sandwich structures and how to use these waves for testing. One main reason is that the energy of the waves gets attenuated significantly inside the honeycomb core and it is difficult to interpret the experimental results [11]. Research has been done using global matrix method for analyzing the wave propagation in honeycomb sandwich structures [12]. Some work using finite element method have also been done for the honeycomb sandwich structures [13]. Damage localization in these structures using mode conversion has been studied experimentally [14, 15]. It can be concluded that there are at least have two different propagation models for the honeycomb sandwich structures: the homogenized model and the discretized model. The homogenized model considered the honeycomb sandwich panel as a three-layered media with the homogenized mechanical

properties, while the discretized model considers that waves mainly propagate inside the excited face sheet and can interact with the core.

1.2 Outline of the thesis

The goal of this thesis is to explore how the Lamb waves behave in thick plates and in layered media at high frequencies. To better present the work, the thesis is split into Chapters 2 - 4, covering the three main topics: theoretical research on Lamb waves in a thick plates and in layered media, and experiments on waves propagating in honeycomb sandwich structures.

Chapter 2 introduces the Lamb wave dispersion equations and solving for the response using residue theory for a homogeneous plate. A new equation roots-search tool is developed in order to find the roots of the dispersion equations efficiently. With this tool, a wide-range of dispersion curves can be obtained and some new wave phenomena are discussed analytically. At the end, the thick plate responses predicted by Lamb wave theory are compared with numerical simulations, and some newly discovered properties are presented.

Chapter 3 discusses several improvements in existing formulas related to the solution of Lamb waves propagating in layered media. First, a new method to obtain the mode shapes using singular value decomposition is proposed. Then a new formula in matrix form is derived to obtain the analytical solution for the wave fields in layered media. A new method to avoid well known singularities in the formulas is proposed. With these new tools, the dispersion curves in homogenized HSS structure is obtained. Research is conducted on studying the effects of the homogenized core properties to the dispersion curves of the HSS structure. And finally, the Q-factor-based damping model is validated in experimentally and can potentially be used in the NDE of HSS.

Chapter 4 presents several experimental studies on Lamb waves in honeycomb sandwich structures and discusses how they can be used in damage detection. A new damage index is proposed together with an improved mapping method for detecting a core-skin disbond damage in a honeycomb sandwich structures. Then a feasibility study is conducted in using non-contact air-coupled transducers to detect damages in honeycomb sandwich structures.

Chapter 2 Lamb Waves in a Thick Plate

2.1 Lamb wave dispersion equations and responses in an homogeneous isotropic plate

Consider an isotropic plate of thickness 2*H* shown in Figure 2-1, together with a global coordinate system in which X and Z axes are parallel to the plate surfaces and the Y- axis is normal to the plate. A plane strain problem on the XY-plane is considered in this study.

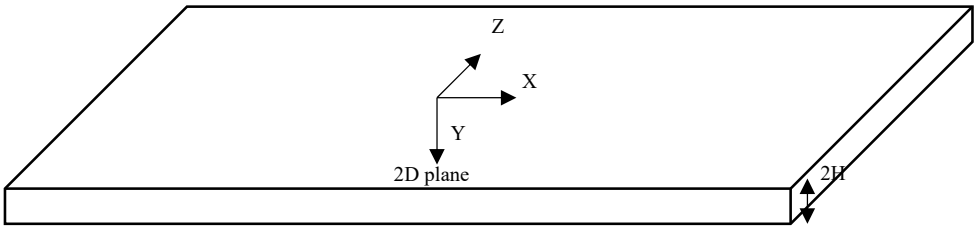

Figure 2-1 Coordinate system in an isotropic plate

By solving the equations of motion using the Helmholtz's decomposition and substituting the displacements into the boundary conditions, one can obtain the dispersion equations [16]

$$\begin{cases} \dfrac{\tanh(\eta_2 H)}{\tanh(\eta_1 H)} = \dfrac{(k^2+\eta_2^2)^2}{4k^2\eta_1\eta_2} \\ \dfrac{\tanh(\eta_1 H)}{\tanh(\eta_2 H)} = \dfrac{(k^2+\eta_2^2)^2}{4k^2\eta_1\eta_2} \end{cases} \tag{2-1}$$

where $\eta_i = \sqrt{k^2 - k_i^2}$, $k_i = \frac{\omega}{c_i}$, $c_1 = \sqrt{\frac{\lambda+2\mu}{\rho}}$ and $c_2 = \sqrt{\frac{\mu}{\rho}}$ and λ, μ are the Lame constants of the solid.

The displacement and stress in the plate can be expressed in the form:

$$\begin{cases} u = -\dfrac{1}{4\pi^2}\iint \dfrac{ikP(\omega,k)}{2\mu R_s}[(2k^2-k_2^2)\cosh(\eta_1 y)\sinh(\eta_2 H) - 2\eta_1\eta_2\sinh(\eta_1 H)\cosh(\eta_2 y)]e^{i(kx-\omega t)}dkd\omega \\ v = -\dfrac{1}{4\pi^2}\iint \dfrac{\eta_1 P(\omega,k)}{2\mu R_s}[(2k^2-k_2^2)\sinh(\eta_1 y)\sinh(\eta_2 H) - 2k^2\sinh(\eta_1 H)\sinh(\eta_2 y)]e^{i(kx-\omega t)}dkd\omega \\ \sigma_{xx} = \dfrac{1}{4\pi^2}\iint \dfrac{P(\omega,k)}{2R_s}[(k_2^2+2\eta_1^2)(2k^2-k_2^2)\cosh(\eta_1 y)\sinh(\eta_2 H) - 4k^2\eta_1\eta_2\sinh(\eta_1 H)\cosh(\eta_2 y)]e^{i(kx-\omega t)}dkd\omega \\ \sigma_{zz} = -\dfrac{1}{4\pi^2}\iint \dfrac{P(\omega,k)}{2R_s}[(2k^2-k_2^2)^2\cosh(\eta_1 y)\sinh(\eta_2 H) - 4k^2\eta_1\eta_2\sinh(\eta_1 H)\cosh(\eta_2 y)]e^{i(kx-\omega t)}dkd\omega \\ \sigma_{xz} = -\dfrac{1}{4\pi^2}\iint \dfrac{(2k^2-k_2^2)\eta_1 ikP(\omega,k)}{R_s}[\sinh(\eta_1 y)\cosh(\eta_2 H) - 2k^2\cosh(\eta_1 H)\sinh(\eta_2 y)]e^{i(kx-\omega t)}dkd\omega \end{cases} \tag{2-2}$$

for the symmetric modes and

$$\begin{cases} u = -\dfrac{1}{4\pi^2}\iint \dfrac{ikP(\omega,k)}{2\mu R_A}[(2k^2-k_2^2)\sinh(\eta_1 y)\cosh(\eta_2 H) - 2\eta_1\eta_2\cosh(\eta_1 H)\sinh(\eta_2 y)]e^{i(kx-\omega t)}dkd\omega \\ v = -\dfrac{1}{4\pi^2}\iint \dfrac{\eta_1 P(\omega,k)}{2\mu R_A}[(2k^2-k_2^2)\cosh(\eta_1 y)\cosh(\eta_2 H) - 2k^2\cosh(\eta_1 H)\cosh(\eta_2 y)]e^{i(kx-\omega t)}dkd\omega \\ \sigma_{xx} = \dfrac{1}{4\pi^2}\iint \dfrac{P(\omega,k)}{2R_A}[(k_2^2+2\eta_1^2)(2k^2-k_2^2)\sinh(\eta_1 y)\cosh(\eta_2 H) - 4k^2\eta_1\eta_2\cosh(\eta_1 H)\sinh(\eta_2 y)]e^{i(kx-\omega t)}dkd\omega \\ \sigma_{zz} = -\dfrac{1}{4\pi^2}\iint \dfrac{P(\omega,k)}{2R_A}[(2k^2-k_2^2)^2\sinh(\eta_1 y)\cosh(\eta_2 H) - 4k^2\eta_1\eta_2\cosh(\eta_1 H)\sinh(\eta_2 y)]e^{i(kx-\omega t)}dkd\omega \\ \sigma_{xz} = -\dfrac{1}{4\pi^2}\iint \dfrac{(2k^2-k_2^2)\eta_1 ikP(\omega,k)}{R_A}[\cosh(\eta_1 y)\sinh(\eta_2 H) - 2k^2\sinh(\eta_1 H)\cosh(\eta_2 y)]e^{i(kx-\omega t)}dkd\omega \end{cases} \tag{2-3}$$

for the antisymmetric modes. $P(\omega, k)$ is the surface loading after taking double Fourier transform with respect to time t and coordinate x. R_S and R_A can be expressed by:

$$\begin{cases} R_a(\omega,k) = 4k^2\eta_1\eta_2\cosh(\eta_1 H)\sinh(\eta_2 H) - (k^2+\eta_2^2)^2\sinh(\eta_1 H)\cosh(\eta_2 H) \\ R_s(\omega,k) = 4k^2\eta_1\eta_2\sinh(\eta_1 H)\cosh(\eta_2 H) - (k^2+\eta_2^2)^2\cosh(\eta_1 H)\sinh(\eta_2 H) \end{cases} \tag{2-4}$$

The roots $k(\omega)$ for (2-1) need to be solved by numerical tools. After obtaining the roots, the displacements and stresses can be solved by substituting k into the expressions. The following subchapters focuses on the equation solver and responses for a thick plate under high frequency excitations.

2.2 Self-adapted root searcher

The dispersion equations are transcendental and periodic equations, whose roots cannot be found easily. Till these days, numerical methods are widely used to solve the equations to obtain the dispersion curves for different solids and structures. They include the superposition of partial bulk waves (SPBW), semi-analytical finite element (SAFE) method, wave-guide finite element (WFE) method [24-28]. However, these numerical methods do not work very well at higher frequencies or for large plate thickness since they are tied to the mesh size of each element. There are also several analytical solvers for this problem, one of them is by using a tracing algorithm [17]. However, it has been found that this algorithm can become unstable when the dispersion curves is unstable when the slope of the dispersion curves is too large or too small. There are many other methods such as Muller's method to obtain the solution of a complex transcendental equation. However, due to the algebraic complexity of the dispersion equations, it is difficult to obtain the solution accurately and efficiently, especially in the high frequency region (more than 10MHz) where there are much larger number of modes compared to the low frequency region. To adapt the complicated situation of the dispersion curves, a self-adapted root

searcher is developed. This subchapter mainly introduces the searcher in three topics: the root judging method, the initial roots searching and the root tracing algorithm.

2.2.1 Root judging method

For convenience, in the following part of the thesis, the evaluated function value is expressed in the form (*Re*, *Im*), where *Re* is the real part of the evaluated function and *Im* is the imaginary part. In order to search and find the solution, the dispersion equations are rewritten into continue functions form to remove the singularities in *tan* function, and the problem reduces to finding the roots of continuous functions in equation (2-4).

The roots for the function are at the point with magnitude 0. Numerically speaking, the closest point to the root of the function within the searching range will have the minimum magnitude. However, the point with the minimum magnitude within the searching range may not always be the solution. Therefore, a new method to judge the root of the equation is needed for the searcher. It is shown that the function near the root are three types: “I” shape, “U” shape and “L” shape.

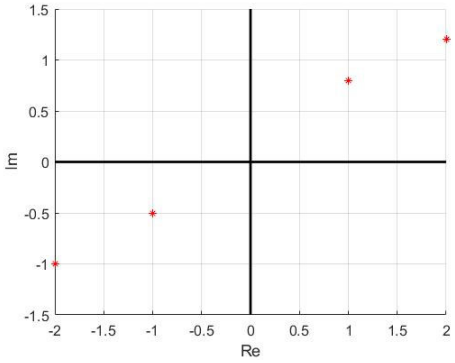

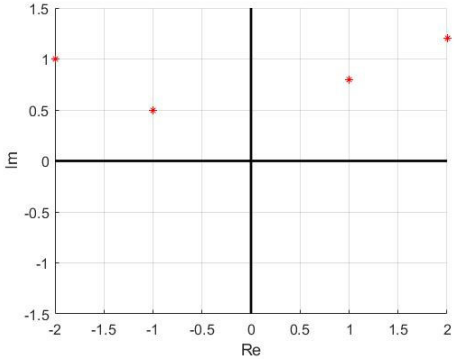

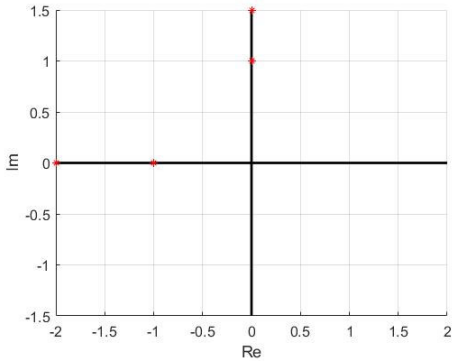

Figure 2-2 The three types of the distribution of the evaluated function values near a root, (a) "I" shape (b) "U" shape and (c) "L" shape

Figure 2-2 shows the three types of the distributions. The "I" shaped distribution includes a pure real or imaginary solution. It happens when the root is in an odd order. The function near the root crosses the diagonal quadrants. It usually happens for fundamental modes or when the frequency is very large. This can be summarized using the mathematical expression:

$$Re(f_n)Re(f_{n+1}) \leq 0 \bigcap Im(f_n)Im(f_{n+1}) \leq 0 \tag{2-5}$$

The "U" shape appears when the root is in an even order. The function crosses two neighboring quadrants. It happens for higher modes when the wave number is low and can be expressed by:

$$Re(f_n)Re(f_{n+1}) \leq 0 \bigcap Im(f_{n-1} - f_n)Im(f_{n+1} - f_{n+2}) < 0$$

or

$$Im(f_n)Im(f_{n+1}) \leq 0 \bigcap Re(f_{n-1} - f_n)Re(f_{n+1} - f_{n+2}) < 0 \tag{2-6}$$

Lastly, the “L” shape happens when the function has a branch cut, and the evaluated function values changes from pure real numbers to pure imaginary numbers. This usually happens when the dispersion curves pass through the Bulk wave velocity c_1 and c_2. It can be expressed by:

$$Re(f_n)Re(f_{n+1}) = Im(f_n)Im(f_{n+1}) = 0 \tag{2-7}$$

All evaluated values within the searching range will be checked by the method above and any sampling point that satisfied any of the three cases will be considered as a solution of the Lamb waves dispersion equations.

2.2.2 Root searching

To initiate the searching, the initial searching limits are defined. A low frequency limit is defined to search for the roots of all fundamental modes. The limit cannot be zero since dispersion equations are singular at frequency equals to zero. The initial searching range is divided into hundreds of uniform or non-uniform intervals, based on the goal of the searching engine. If the searching engine is for searching $\omega - k$ domain, the intervals will be non-uniform when searching for k. Instead, the ω/k values, which is the phase velocities, searching intervals are uniform. By doing this, one can avoid the crowded k values when ω is small. After finding the possible intervals which contain roots, the target interval will be then divided into even smaller intervals for increasing the accuracy. The same operation will be repeated until the interval length reaches the requirements, and then the beginning data of the target interval will be considered as the root.

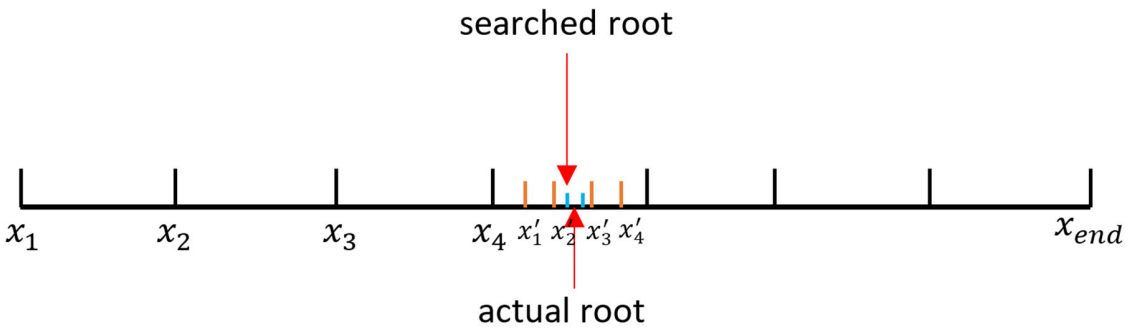

Figure 2-3 Searching for the initial roots of the equation

The root judging method requires 4 data points for the input: f_{n-1} to f_{n+2}. If $n = 1$ or $n \geq end - 1$, which means the root happens on the boundary of the searching range, an additional value will be introduced to guarantee four values inputting into the root judging method. For example, if $n = 1$, a value with the index $n = 0$ will be introduced and $x_2 - x_1 = x_1 - x_0$ is guaranteed.

2.2.3 Root tracing algorithm

To guarantee that the root exists within the searching range, a local polar coordinate is set up for searching the root. Two variables are defined for searching the root: searching radius and searching angle. Starting from the initial roots, a searching range with 180 degrees of searching angle is applied. Once the next root is found, based on the previous two root, the algorithm will predict the next searching range by considering this function is close to linear within a small range. After the first three roots are found, based on the slope change, the searching angle and searching radius will be adjusted. For a small slope change, the searching angle will be smaller, and the searching radius will be larger, to efficiently compute the following roots. For a large

slope change, the searching angle will be larger, and the searching radius will be smaller, to increase the accuracy of the solution sets. A flowchart of the algorithm and its schematic graph are shown in Figs. 2-4 and 2-5.

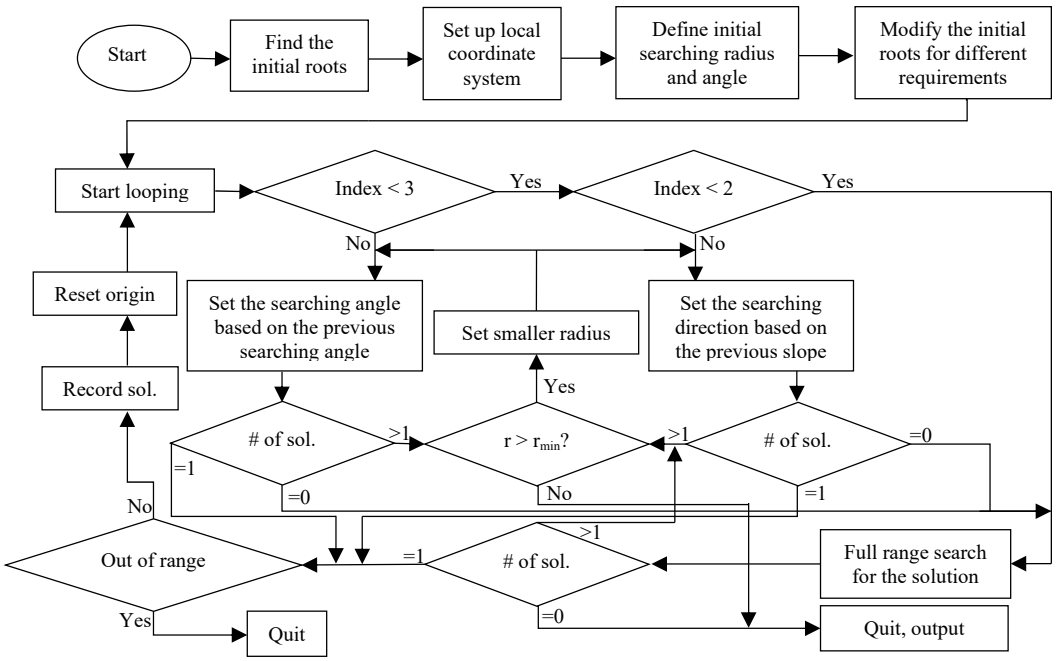

Figure 2-4 Flowchart of the Algorithm

There are three types of errors that may happen during the searching process. The first type shows that there is no solution within the searching range. This usually happens when the dispersion curves cross one another or when the searching angle is too small. The second type is that multiple solutions are found within the searching range. This type of error happens when the searching radius is too large and when two modes are close to each other. The third type is that the root is closed to the boundary. This occurs when the slopes of the dispersion curves change significantly. If the first two types happen, then the searching radius will be reduced, and the

searching angle will increase. If no solution can be found with the full range search which has the maximum accuracy, the program will quit and report the error information to the user.

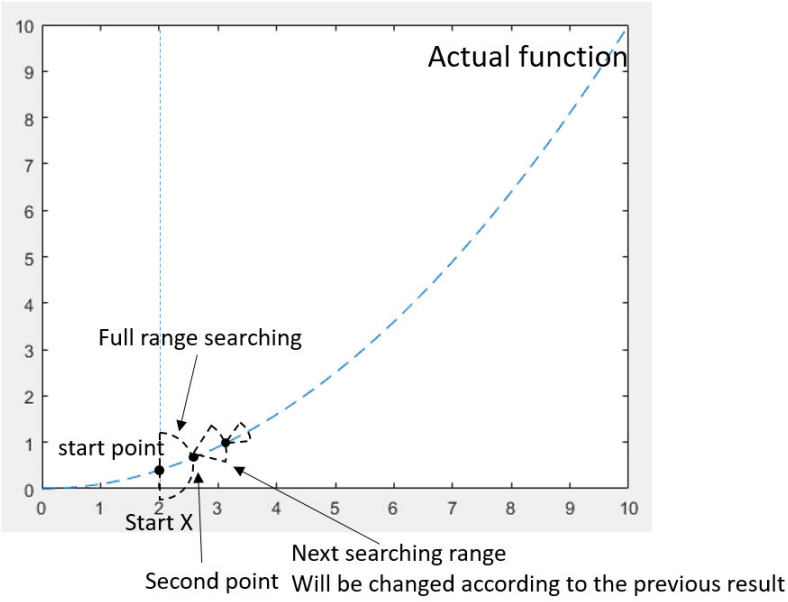

Figure 2-5 Schematic Graph for the Algorithm

2.3 Dispersion curves in a wide frequency range

With the efficient searcher, the dispersion curves in a wide frequency range can be determined and studied. In this subsection, the behavior of the dispersion curves for an aluminum plate under a wide frequency range will be studied, including the cut-off frequencies and the convergence property of different modes.

2.3.1 Cut-off frequencies

Equation (2-1) shows the dispersion equations for the Lamb waves including the symmetric and antisymmetric modes. These equations can be expressed in the alternate forms:

$$\begin{cases} \dfrac{\tanh(v_2\Omega)}{\tanh(v_1\Omega)} = \dfrac{(v^2+v_2^2)^2}{4v^2v_1v_2} \\ \dfrac{\tanh(v_1\Omega)}{\tanh(v_2\Omega)} = \dfrac{(v^2+v_2^2)^2}{4v^2v_1v_2} \end{cases} \tag{2-8}$$

where $\Omega = \omega H$ is the frequency-thickness-product and $v = \frac{1}{c_p}$, $v_i = \sqrt{\frac{1}{c_p} - \frac{1}{c_i}}$, c_p is the phase velocity.

The cut-off frequencies are the frequencies when new modes start to appear. All modes start with $k = 0^+$. For the antisymmetric modes, when $k = 0^+$, equation (2-8) can be solved and the cut-off frequencies can be obtained:

$$\begin{cases} \Omega_1 = c_1 n\pi \\ \Omega_2 = c_2\left(n\pi - \dfrac{\pi}{2}\right) \end{cases} \tag{2-9}$$

where n is an integer. Notice that in equation (2-9) there are two families of roots having different periods, and therefore the root is not periodical.

Similar to the antisymmetric modes, the symmetric modes have the cut-off frequencies given by:

$$\begin{cases} \Omega = c_2 n\pi \\ \Omega = c_1\left(n\pi + \dfrac{\pi}{2}\right) \end{cases} \tag{2-10}$$

The cut-off frequencies in equation (2-10) are plotted together with the dispersion curves in the Ω-k plane in Figure 2-6.

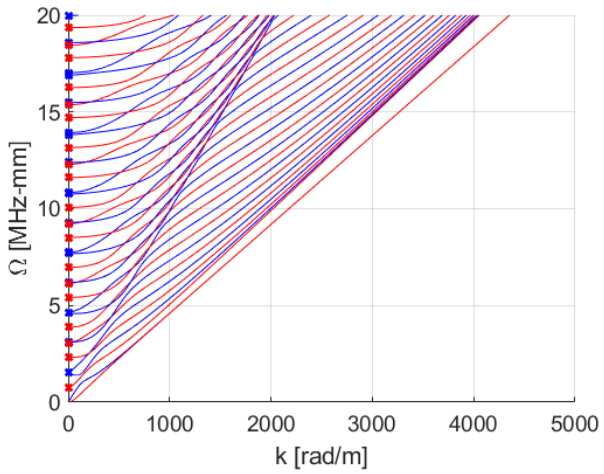

Figure 2-6 Dispersion curves and the predicted cut-off frequencies

2.3.2 Convergence study

The phase velocity of the Lamb waves will converge to some specific values when the frequency-thickness-product tends to infinity. When the convergence velocity is lower than c_2, both v_1 and v_2 will be real numbers, and therefore, $\tanh(v_i\Omega) \to 1$ and (2-8) becomes:

$$(v^2 + v_2^2)^2 - 4v^2 v_1 v_2 = 0 \tag{2-11}$$

Equation (2-11) shows one convergence velocity for both symmetric and antisymmetric modes. It is clear that when the frequency-thickness-product is large, the solution is unique, implying that there is only one mode for each family that converges to this velocity. This velocity is equal to the Rayleigh wave velocity c_r in the same solid.

If the convergence velocity is higher than c_2 but lower than c_1, $\tanh(v_2\Omega)$ in (2-11) becomes $\tanh(is_2\Omega) = itan(s_2\Omega)$, where $s_2 = -iv_2$ is a real number. When Ω is large enough, $\tanh(v_1\Omega) \to 1$ and (2-8) can be transformed to:

$$\begin{cases} \tan(s_2\Omega) = -\dfrac{(v^2 - s_2^2)^2}{4v^2 v_1 s_2} = f(s_2) \\ \cot(s_2\Omega) = \dfrac{(v^2 - s_2^2)^2}{4v^2 v_1 s_2} = -f(s_2) \end{cases} \tag{2-12}$$

Notice that when s_2 is a fixed number (i.e., when c_p is a constant), the frequency-thickness product for high frequencies can be expressed as:

$$\begin{cases} \Omega = \dfrac{\arctan\big(f(s_2)\big) + n\pi}{s_2} \\ \Omega = \dfrac{\arctan\big(f(s_2)\big) + \left(n + \dfrac{1}{2}\right)\pi}{s_2} \end{cases} \tag{2-13}$$

Equation (2-13) provide the solutions of the dispersion equations for large frequency-thickness-product representing different modes. It can be observed that if the frequency-thickness product is large enough, the symmetric modes and anti-symmetric modes appear to be periodic functions with a period of $\frac{\pi}{s_2}$. Furthermore, the separation distance between two neighboring modes is $\frac{\pi}{2s_2}$. Notice that when $s_2 \to 0$, meaning that $c_p \to c_2$, the distance between two modes, $\frac{\pi}{2s_2}$, approaches ∞. This means that the two modes will never intersect with each other when they are approaching c_2.

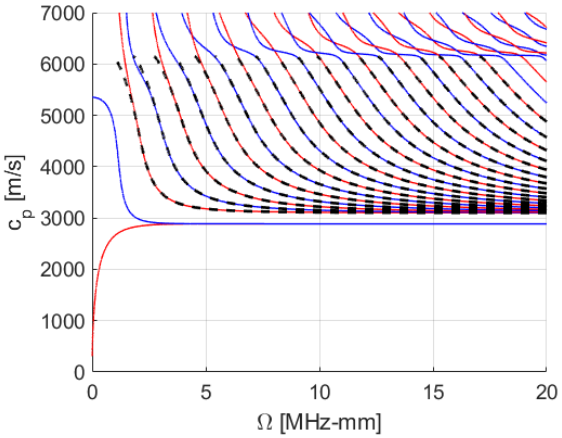

Figure 2-7 Comparison between the solution of the exact equations with those obtained from the approximate simplified equations. The blue lines are for the symmetric mode, red lines are for the antisymmetric modes and black dashed lines are for the approximate solutions

If the convergence velocity is higher than c_1, $s_i = -iv_i$ is a real number and the equation becomes $\tanh(is_i\Omega) = itan(s_i\Omega)$. Then equations (2-8) can be rewritten as:

$$\begin{cases} \dfrac{\tan(s_2\Omega)}{\tan(s_1\Omega)} = -\dfrac{(v^2 - s_2^2)^2}{4v^2 s_1 s_2} = g(c_p) \\ \dfrac{\tan(s_1\Omega)}{\tan(s_2\Omega)} = -\dfrac{(v^2 - s_2^2)^2}{4v^2 s_1 s_2} = g(c_p) \end{cases} \tag{2-14}$$

The transcendental equations are usually unsolvable with only assuming Ω is large. However, unlike the previous results, the symmetric modes and antisymmetric modes can cross over each other, and the cross-points are given by:

$$\tan^2(s_1\Omega) = \tan^2(s_2\Omega) \tag{2-15}$$

From equation (2-14), it is obvious that $g(c_p)$ is a function with only negative real values, implying that $\tan(s_1\Omega)$ and $\tan(s_2\Omega)$ must have different sign. Therefore, equation (2-15) can be transformed into:

$$R(c_p) = s_1 + s_2 = \frac{n\pi}{\Omega} \tag{2-16}$$

and the frequency can be expressed as:

$$\Omega = \frac{n\pi}{\sqrt{\frac{1}{c_1^2} - \frac{1}{c_p^2}} + \sqrt{\frac{1}{c_2^2} - \frac{1}{c_p^2}}} \tag{2-17}$$

Equation (2-17) represents the asymptote line that all the cross points of symmetric and antisymmetric modes pass through. It is shown that when the frequency-thickness-product increases, the symmetric modes and antisymmetric modes get closer and closer to the asymptote line.

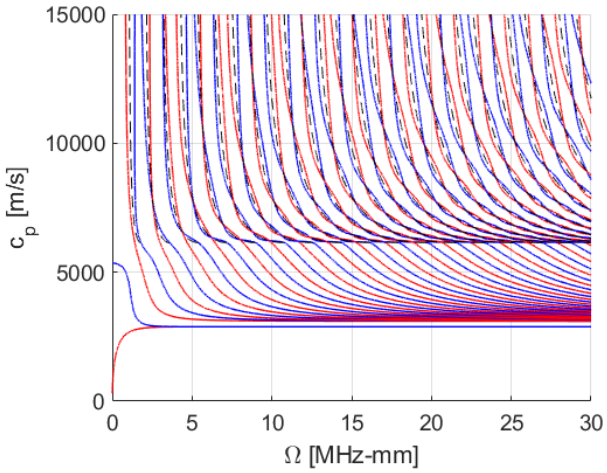

Figure 2-8 Symmetric modes (blue lines), antisymmetric modes (red lines) and the asymptotes (black dashed line)

2.4 Thick plate response compared with finite element simulation

With the efficient tools to obtain dispersion curves, the force responses can be expanded to a wide frequency range. In this chapter, the high frequency responses of the Lamb waves are discussed and the solutions from different methods are compared. The Lamb waves responses are compared to the numerical solution obtained by finite element simulation of a thick block.

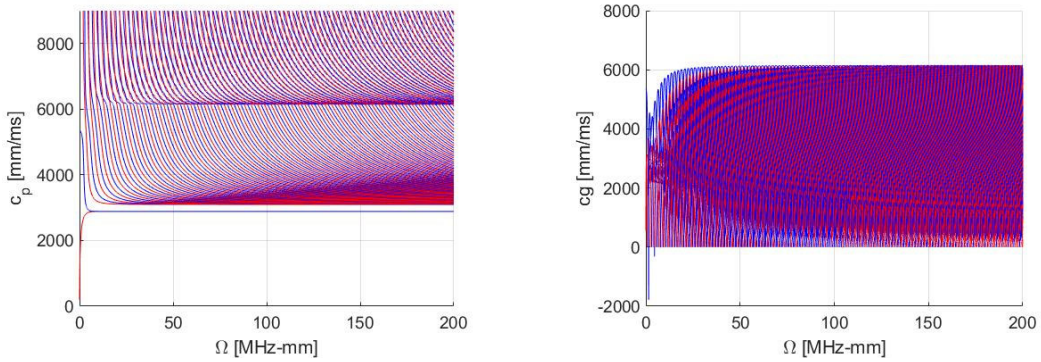

Figure 2-9 Dispersion curves for a wide range of frequencies a) phase velocity b) group velocity

2.4.1 Lamb wave prediction at large frequency-thickness product

Using equation (2-2) and (2-3), the displacements components within the plate can be obtained. Some results are shown in the following figures:

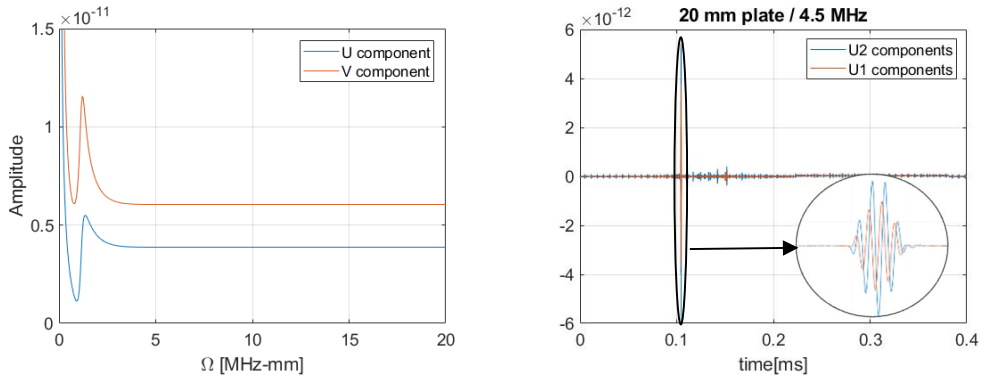

Figure 2-10 Responses of the top surface a) in frequency domain for only the fundamental modes and b) in time domain

When the frequency is high, the response of the plate converges to that of a semi-infinite plate response. It can be seen from Figure 2-10 b) that the response includes the Rayleigh wave (the main packet) and other waves reflected from the boundary of the numerical model. According to the analytical solution of the semi-infinite medium, for the Rayleigh wave amplitudes in the horizontal displacement should be roughly $2/3$ of the vertical displacement. This can be seen also from the results for Lamb waves at very high frequencies presented in Figure 2-10. Moreover, the phase and group velocities of the fundamental modes also converge to the Rayleigh wave velocity. It is reasonable to assume that the fundamental modes will be converted to Rayleigh waves with increasing values of frequency and thickness product. The amplitude of the sum of two fundamental modes across the thickness of the plate is presented in Figure 2-11 a). It can be seen that near the surface, the amplitude decay exponentially, which is expected to be seen in a Rayleigh wave. From Figure 2-11 b) it can be seen from the time domain signals that the summation of two fundamental modes can form a clear signal who has the velocity of the Rayleigh wave.

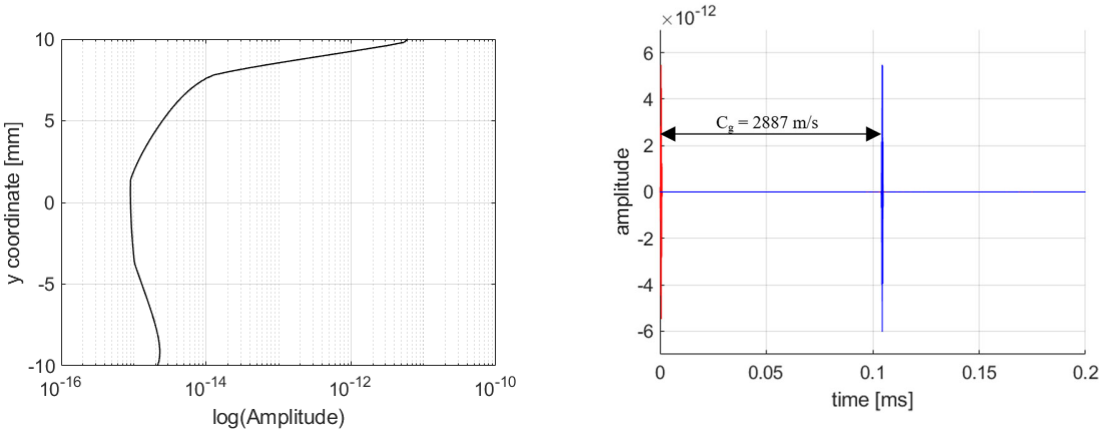

Figure 2-11 Summation of two fundamental modes shown as a) through-thickness amplitude profile and b) time domain signal

Next, to further study the high frequency solution, some parts of the solution are removed from the original solution of the dispersion equations. The remaining solution satisfies the following relationship:

$$c_p = \frac{\omega}{k} \leq 0.99\, c_1 = 0.99 \sqrt{\frac{\lambda + 2\mu}{\rho}} \tag{2-18}$$

With this condition, all data that contain phase velocity greater than c_1 is filtered out. Then the displacements at $x = 17.4mm$ and $y = 0$ (midplane) is obtained for comparison. The results are shown in Figure 2-12. It can be concluded that with the modification, the P wave(first packet) is removed from the original response. Conclusion can be dropped that for a wide frequency range response, instead of studying the motion of certain modes, studying the combination of all modes may be physically more meaningful.

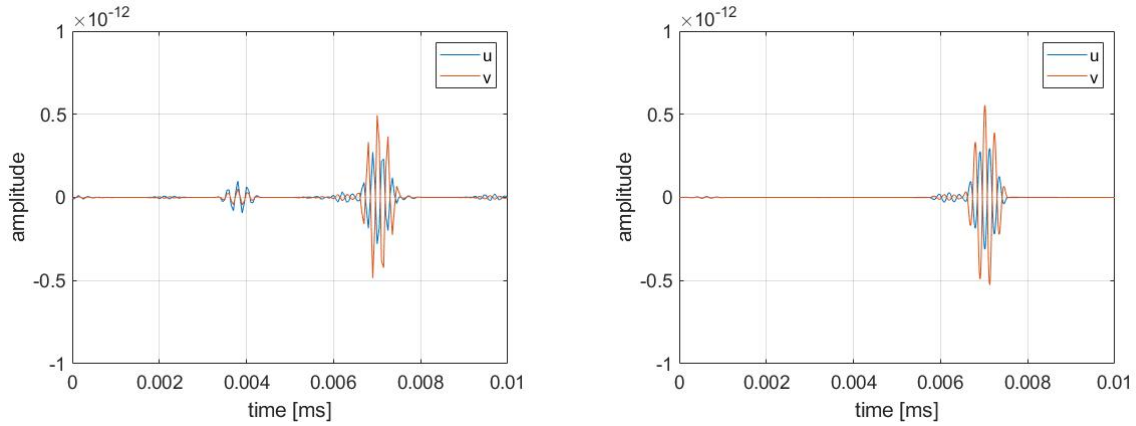

Figure 2-12 Displacements at $x = 17.4mm$ and $y = 0$ for a) without modification and b) with modification

2.4.2 Finite element results

Finite element method is commonly used to obtain the wavefield of the solution. To verify the theoretical result obtained from the previous subchapters, a finite element model is constructed in order to compare with the theoretical solution. The model is $20\text{mm} \times 40\text{mm}$ in size and the historical result is presented at the coordinate $x = 13.5mm$ and $y = 0$. The material is aluminum with the material properties given below.

Mechanical Properties	E [GPa]	ν	ρ [kg/m^3]
	68.9	0.33	2700

Table 2-1 Material properties of Aluminum 6061-T6

The shear wave velocity for this solid is $3097\ \text{mm/ms}$ and the corresponding wavelength under an excitation of 4.5 MHz is about 0.69 mm. To guarantee at least 20 elements per wavelength, the mesh size is selected to be 0.025 mm. As for the time increment, the sampling frequency is selected to be 200 MHz, more than 40 times of the central frequency of the signal to guarantee convergence. Plane strain element is used for the calculation and the dynamic explicit procedure is used. The solution is then compared to the theoretical Lamb wave prediction.

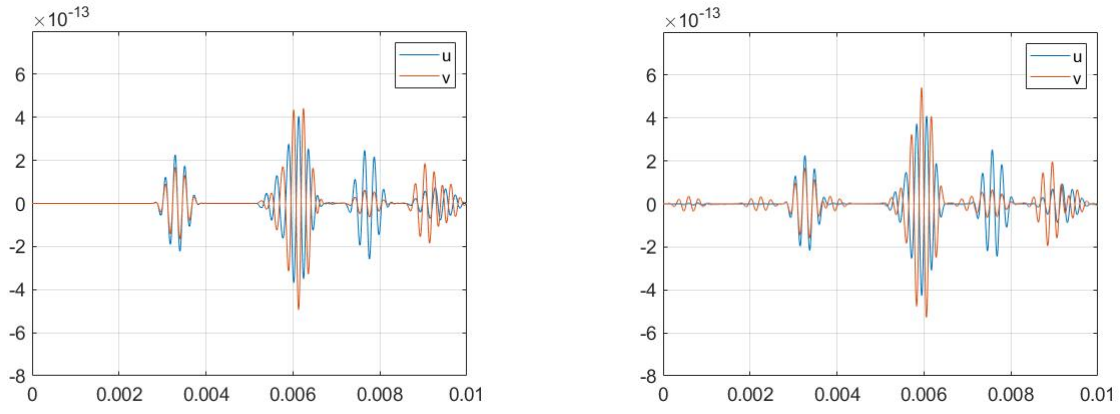

Figure 2-13 Response at $x = 13.5mm$ and $y = 0$ for a) FEM simulation and b) Lamb wave prediction

Figure 2-13 shows a comparable result between the FEM simulation and Lamb wave prediction. The difference includes: 1) There is resonance in the Lamb wave prediction due to the numerical instability near the cut-off frequencies. 2) In general, the time of arrival of each packet is identical. 3) There are small differences between the predicted and simulated results. The difference may have resulted from the fact that the two cases are not exactly the same in term of the loading.

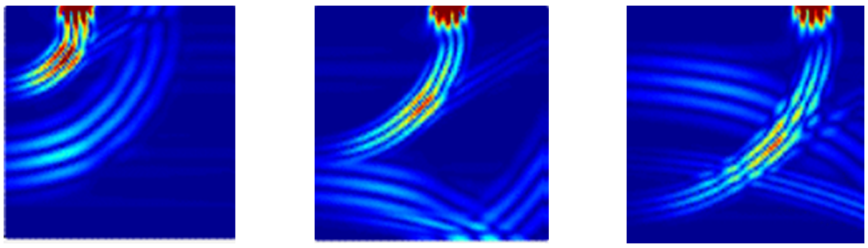

Figure 2-14 Lamb-wave predicted field output for a point source

Chapter 3 Lamb Waves in Layered Media

In 1917, Lamb H. first provided the theory on wave propagation inside an elastic plate [18]. It was shown that for waves propagating inside a plate, there exists dispersion phenomenon in velocity and the dispersion equation was derived. Since then, elastic wave propagation in a solid plate became a hot topic in seismology and earthquake studying. In 1950, Thomson proposed a [19] matrix manipulation of elastic wave problems and later Haskell corrected and elaborated the method [20]. The Thomson matrix method also be is referred as Transfer Matrix Method (TMM) for solving the dispersive relation in a multilayered medium. However, research shows that TMM does not have a good stability of the mode decaying through the thickness [21], especially for large thickness or high frequency. Later in 1964, Knopoff provide an alternate matrix method, and later known as Global Matrix Method (GMM), to provide a relatively robust solution for the dispersion equation in layered media [22]. The method is latter improved by changing of local coordinate system, which greatly reduced the numerical error [23]. Since then, GMM is widely used for analysis the dispersion relations in composite layered material. There are other methods and studies on obtaining the elastodynamic response of layer media such as the Elastodynamic Green's function [36-39], numerical method [24, 25]. This thesis focuses on the global matrix method, and the method of residue to obtain the forcing response, for its advantage in obtaining accurate high frequency results while keeping the computational efficiency.

3.1 The global matrix method

Consider an isotropic plate shown in Figure 3-1 with the thickness H. The global coordinate system is set so that X and Z are the in-plane coordinates and Y are the out of plane direction. The

plane formed by *X* and *Y* coordinates are the 2D plane of interest. For this case, the plane can be considered as plane strain problem as the *Z* direction dimension is relatively large. By considering the equilibrium equations inside elastic solid material and applying proper boundary condition, one can obtain the elastic wave propagation matrix, which will be shown in the following chapter.

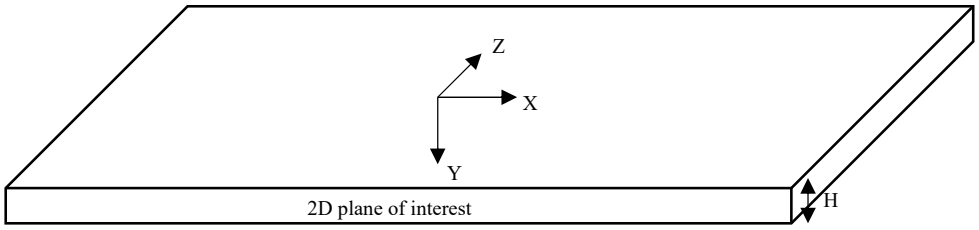

Figure 3-1 Global coordinate system in isotropic plate

3.1.1 Potential functions and solution in local layer

For a homogeneous and isotropic solid material with plane strain assumption, with small displacements, the 2D stress component inside the plane of interest can be express in terms of linear combinations of first partial derivatives of displacement, also known as Hooke's law for elasticity:

$$\begin{Bmatrix} \sigma_x \\ \sigma_y \\ \tau_{xy} \end{Bmatrix} = \begin{bmatrix} \lambda + 2\mu & \lambda & 0 \\ \lambda & \lambda + 2\mu & 0 \\ 0 & 0 & \mu \end{bmatrix} \begin{Bmatrix} u_{,x} \\ v_{,y} \\ u_{,y} + v_{,x} \end{Bmatrix} \tag{3-1}$$

Displacement can be decomposed by scalar and vector potentials, which is known as Stokes-Helmholtz decomposition:

$$\begin{cases}\mathbf{u}_1 = \varphi_{,x} - \boldsymbol{\psi}_{x,y} \\ \mathbf{u}_2 = \varphi_{,y} + \boldsymbol{\psi}_{y,x}\end{cases}$$

$$\mathbf{u} = \mathbf{u}_1 + \mathbf{u}_2 = \boldsymbol{\nabla}\varphi + \boldsymbol{\nabla} \times \boldsymbol{\psi}$$

(3-2)

Now consider the equations of motion inside an elastic media for plane problem. Assume the media is homogeneous with constant density ρ.

$$\frac{\partial \sigma_x}{\partial \mathrm{x}} + \frac{\partial \tau_{xy}}{\partial \mathrm{y}} = \rho \frac{\partial^2 \mathrm{u}_1}{\partial \mathrm{t}^2}$$
$$\frac{\partial \tau_{xy}}{\partial \mathrm{x}} + \frac{\partial \sigma_y}{\partial \mathrm{y}} = \rho \frac{\partial^2 \mathrm{u}_2}{\partial \mathrm{t}^2}$$

(3-3)

By substituting (3-1) and (3-2) into (3-3), one can obtain the set of equations for the potential functions for an elastic plane strain media:

$$\boldsymbol{\nabla}\left(c_1^2 \Delta\varphi - \frac{\partial^2 \varphi}{\partial \mathrm{t}^2}\right) + \boldsymbol{\nabla} \times \left(c_2^2 \Delta\boldsymbol{\psi} - \frac{\partial^2 \boldsymbol{\psi}}{\partial \mathrm{t}^2}\right) = 0$$

(3-4)

One of the solution set for the two potential functions is:

$$\begin{cases} c_1^2 \Delta\varphi - \dfrac{\partial^2 \varphi}{\partial \mathrm{t}^2} = 0 \\ c_2^2 \Delta\boldsymbol{\psi} - \dfrac{\partial^2 \boldsymbol{\psi}}{\partial \mathrm{t}^2} = \mathbf{0} \end{cases}$$

(3-5)

Where:

$$c_1 = \sqrt{\frac{\lambda + 2\mu}{\rho}}, \quad c_2 = \sqrt{\frac{\mu}{\rho}}$$

Finally the potential functions can be obtain by solving the second order partial differential equation. For convenience, the potential function is split into a function of time multiplied by a function of space:

$$\begin{cases} \varphi = \mathrm{A}\mathrm{e}^{\mathrm{i}(\mathrm{k}x\pm\eta_1 y)}\mathrm{e}^{-\mathrm{i}\omega t} = \mathrm{A}\varphi^{\pm}(x,y)\mathrm{e}^{-\mathrm{i}\omega t} \\ \boldsymbol{\psi} = \mathbf{B}\mathrm{e}^{\mathrm{i}(\mathrm{k}x\pm\eta_2 y)}\mathrm{e}^{-\mathrm{i}\omega t} = \mathbf{B}\boldsymbol{\psi}^{\pm}(x,y)\mathrm{e}^{-\mathrm{i}\omega t} \end{cases} \tag{3-6}$$

Where:

ω is the angular frequency of the wave

k is the wavenumber in x direction

η_1, η_2 are the wavenumber in y direction and

$$\begin{cases} \eta_1 = \sqrt{k^2 - \frac{\omega^2}{c_1}} \\ \eta_2 = \sqrt{k^2 - \frac{\omega^2}{c_2}} \end{cases} \tag{3-7}$$

Finally, by substituting the potential function expression in (3-6) into (3-1) and (3-2), one can obtain the displacement and stress solution for one layer:

$$\begin{cases} u = (ikC_1\varphi^{-}(x,y) + \eta_2 C_2\boldsymbol{\psi}^{-}(x,y) + ikC_3\varphi^{+}(x,y) - \eta_2 C_4\boldsymbol{\psi}^{+}(x,y))\mathrm{e}^{-\mathrm{i}\omega t} \\ v = (-\eta_1 C_1\varphi^{-}(x,y) + \mathrm{i}kC_2\boldsymbol{\psi}^{-}(x,y) + \eta_1 C_3\varphi^{+}(x,y) + \mathrm{i}kC_4\boldsymbol{\psi}^{+}(x,y))\mathrm{e}^{-\mathrm{i}\omega t} \\ \sigma_y = (-2ik\eta_1\mu C_1\varphi^{-}(x,y) - \zeta_2\mu C_2\boldsymbol{\psi}^{-}(x,y) + 2ik\eta_1\mu C_3\varphi^{+}(x,y) - \zeta_2\mu C_4\boldsymbol{\psi}^{+}(x,y))\mathrm{e}^{-\mathrm{i}\omega t} \\ \tau_{xy} = (\zeta_2\mu C_1\varphi^{-}(x,y) - 2ik\eta_2\mu C_2\boldsymbol{\psi}^{-}(x,y) + \zeta_2\mu C_3\varphi^{+}(x,y) + 2ik\eta_2\mu C_4\boldsymbol{\psi}^{+}(x,y))\mathrm{e}^{-\mathrm{i}\omega t} \end{cases} \tag{3-8}$$

Where $\zeta_2 = 2k^2 - k_2^2$. Rearrange the solution in a matrix form:

$$\mathbf{U}(\mathrm{m}) = \begin{Bmatrix} \mathrm{U} \\ \mathrm{V} \\ \mathrm{T} \\ \Sigma \end{Bmatrix} \mathrm{e}^{\mathrm{i}(\mathrm{kx}-\omega \mathrm{t})} = \mathrm{Q}(\mathrm{m})\mathrm{E}(\mathrm{y},\mathrm{m})\mathrm{C}(\mathrm{m})\mathrm{e}^{\mathrm{i}(\mathrm{kx}-\omega \mathrm{t})}$$

$$\mathrm{Q}(\mathrm{m}) = \left[\begin{array}{cc|cc} ik & \eta_2 & ik & -\eta_2 \\ -\eta_1 & ik & \eta_1 & ik \\ \hline -2ik\eta_1\mu & -\zeta_2\mu & 2ik\eta_1\mu & -\zeta_2\mu \\ \zeta_2\mu & -2ik\eta_2\mu & \zeta_2\mu & 2ik\eta_2\mu \end{array}\right]$$

$$\mathrm{Q}(\mathrm{m}) = \begin{bmatrix} Q_{11}(m) & Q_{12}(m) \\ Q_{21}(m) & Q_{22}(m) \end{bmatrix}$$

$$\mathrm{E}(\mathrm{y},\mathrm{m}) = diag(e^{-\eta_1(y-y_{m-1})} \quad e^{-\eta_2(y-y_{m-1})} \quad e^{-\eta_1(y_m-y)} \quad e^{-\eta_2(y_m-y)})$$

$$C(m) = \begin{Bmatrix} C_1 \\ C_2 \\ C_3 \\ C_4 \end{Bmatrix}$$

(3-9)

Where **U** is the displacement-stress matrix for *m*'s layer, *Q* is a spatial independent matrix, *E* is a diagonal spatial dependent matrix and *C* is the undetermined coefficient. This is the matrix form expression of elastic wave propagation inside a plane strain media.

3.1.2 Boundary conditions in the global matrix method

Now consider the boundary conditions for a layered media shown in Figure 3-2. Global coordinate system is set so that the *X* direction is the wave propagation direction while *Y* is through thickness direction. y_0 to y_N is the y coordinates of each interface from the top surface to the bottom surface.

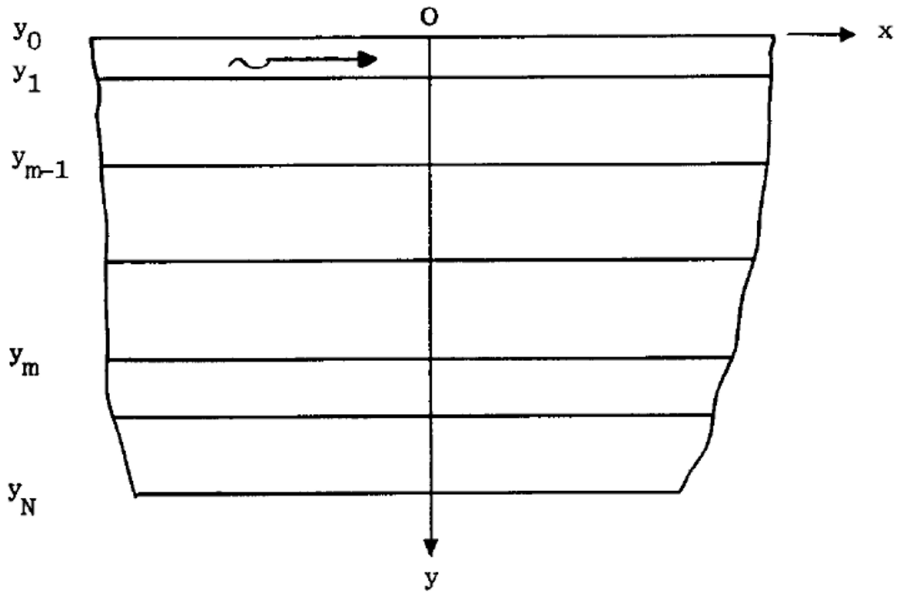

Figure 3-2 Geometry of Layered Media [26]

There are two different types of boundary conditions: traction free boundary conditions at top and bottom surface of the plate and continuity boundary conditions at each interface. The boundary conditions can be expressed as:

$$\begin{cases} \sigma_y = \tau_{xy} = 0 & \text{traction free} \\ \mathbf{U}^+(\mathrm{m}) - \mathbf{U}^-(\mathrm{m}+1) = 0 & \text{continuity condition} \end{cases} \tag{3-10}$$

Where $\mathbf{U}^+$ represents the **U** vector evaluated at the bottom surface (with greater y coordinate) and $\mathbf{U}^-$ represents the **U** vector evaluated at the top surface. According to the coordinate system in Figure 3-2, the spatial dependent matrix *E* evaluated at the surfaces and the interfaces should be written into two sets:

$$\mathrm{E}^+(\mathrm{m}, \mathrm{y_m}) = diag(e^{-\eta_1 h_m} \quad e^{-\eta_2 h_m} \quad 1 \quad 1)$$

$$\mathrm{E}^{-}(\mathrm{m},\mathrm{y}_{\mathrm{m}-1}) = diag(1 \quad 1 \quad e^{-\eta_1 h_m} \quad e^{-\eta_2 h_m})$$

(3-11)

Where h_m is the layer m's thickness and diag() means a diagonal matrix. For convenience, define the E matrix to be:

$$\mathrm{E}(\mathrm{m}) = diag(e^{-\eta_1 h_m} \quad e^{-\eta_2 h_m})$$

(3-12)

So that

$$\mathrm{E}^{+}(\mathrm{m},\mathrm{y}_{\mathrm{m}}) = diag(E(m), I_2)$$
$$\mathrm{E}^{-}(\mathrm{m},\mathrm{y}_{\mathrm{m}-1}) = diag(I_2, E(m))$$

(3-13)

Now substitute (3-11), (3-12) and (3-13) into (3-10), one can obtain the system of equations for the boundary conditions:

$$G\begin{Bmatrix} C_1 \\ C_2 \\ \vdots \\ C_{4N} \end{Bmatrix} e^{i(kx-\omega t)} = GCe^{ik(kx-\omega t)} = 0$$

(3-14)

Where G is the global matrix:

$$G = \begin{Bmatrix} Q_{21}(1) & Q_{22}(1)E(1) & \mathbf{0} & \mathbf{0} & \dots & \mathbf{0} & \mathbf{0} \\ Q_{11}(1)E(1) & Q_{12}(1) & -Q_{11}(2) & -Q_{12}(2)E(2) & \dots & \mathbf{0} & \mathbf{0} \\ Q_{21}(1)E(1) & Q_{22}(1) & -Q_{21}(2) & -Q_{22}(2)E(2) & \dots & \mathbf{0} & \mathbf{0} \\ \vdots & \vdots & \vdots & \vdots & \ddots & \vdots & \vdots \\ \mathbf{0} & \mathbf{0} & \mathbf{0} & \mathbf{0} & \dots & Q_{21}(N)E(N) & Q_{22}(N) \end{Bmatrix}$$

(3-15)

Then a two dimensional Fourier transform about time and space coordinate *x* is applied to the system of equations (3-14) to transform to frequency-wavenumber domain:

$$\iint_{-\infty}^{\infty} GCe^{i(k'x-\omega't)}\, e^{-ikx} e^{i\omega t} dtdx = 0$$

$$\boldsymbol{G}(\omega, k)C = 0$$

(3-16)

From the system of equations in frequency-wavenumber domain (3-16), for a non-trivial solution of *C*, the global matrix *G* should satisfy the equation:

$$\det(\boldsymbol{G}(\omega, k)) = 0$$

(3-17)

Equation (3-17) shows the relationship between frequency ω and wavenumber k, which is also known as dispersion equation of elastic wave propagate inside a layered media.

3.2 Mode shapes obtained from the singular value decomposition

Apart from dispersion curves, the modal function is also a good way to inspect how waves propagate inside a solid. As the results for dispersion curves always have numerical errors, which

makes the computation of modal function much harder. In this chapter, singular value decomposition is applied for an approximate modal function evaluation. Besides, minimum singular value, condition number and null space uniqueness are used to check the stability of different modal functions in different frequency.

3.2.1 Modal functions

To obtain the displacement modal functions, recall the equation (3-9). The displacement modal functions through the thickness in frequency domain should be:

$$\mathbf{U}_{\mathrm{m}}(\omega, \mathrm{y}) = \mathrm{Q}_{1:}(\mathrm{m})\mathrm{E}(\mathrm{y}, \mathrm{m})\mathrm{C}(\mathrm{m}) \tag{3-18}$$

Where:

$$\mathrm{C}(\mathrm{m}) = \mathbf{C}_{(4\mathrm{n}-3):4\mathrm{n}} \text{ and } \mathbf{C} = \mathrm{Null}(\mathbf{G})$$

However, since the numerical searching algorism can't guarantee the $\boldsymbol{G}$ matrix exactly singular, the $\boldsymbol{G}$ matrix computed from the searching result may not have a null space vector. Therefore, by applying the singular value decomposition (SVD) and choose the vector corresponding to the minimum singular value, one can find an approximate null space for global matrix $\boldsymbol{G}$:

$$\mathbf{G} = \mathbf{U}\boldsymbol{\Sigma}\mathbf{V}^{*} = \mathbf{U}\begin{bmatrix}\sigma_1 & \cdots & 0 \\ \vdots & \ddots & \vdots \\ 0 & \cdots & \sigma_{min}\end{bmatrix}\begin{Bmatrix}\boldsymbol{v}_1^{*} \\ \vdots \\ \boldsymbol{v}_c^{*}\end{Bmatrix} \tag{3-19}$$

In the formula, ideally, σ_{min} is the minimum singular value which is supposed to be zero, and $\boldsymbol{v}_c^{*}$ is the complex conjugate transpose of the null space vector of $\boldsymbol{G}$ matrix. As mentioned before, due to the numerical errors, σ_{min} can't be zero and therefore, using $\boldsymbol{v}_c$ as the coefficient vector $\boldsymbol{C}$

will make the solution not satisfying all boundary conditions. But it's still a good approximation for the actual modal function.

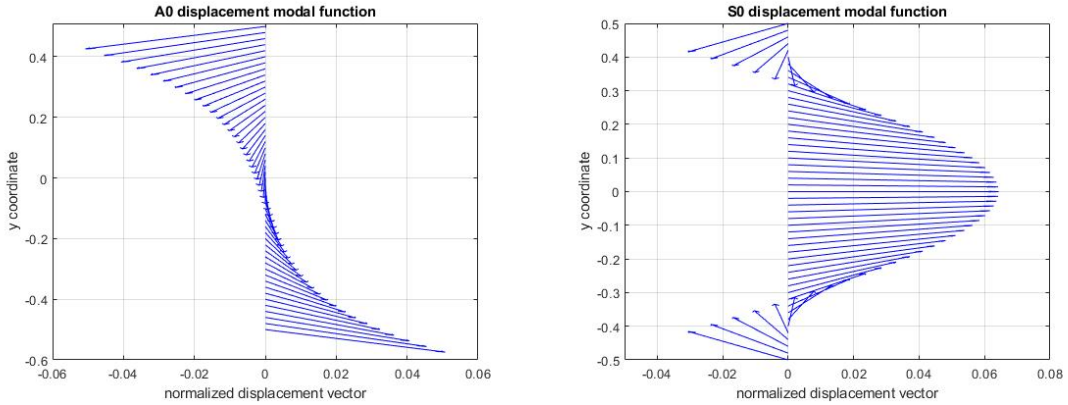

Figure 3-3 Sample A0 and S0 Mode Shapes

3.2.2 Stability control by three important factors

As mentioned before, all boundary conditions cannot be satisfied due to numerical error when finding roots for dispersion equation. Therefore, three factors are used for evaluate the numerical error for different modes under different frequencies: the minimum singular value σ_{min}, the condition number κ and the null space uniqueness ξ. The minimum singular value σ_{min} is the most straight-forward way to evaluate the matrix singularity. When the global matrix is singular, σ_{min} is supposed to be zero. The condition number κ of the global matrix is defined as $\kappa = \frac{\sigma_{max}}{\sigma_{min}}$. It should be close to infinity if the matrix is close to singular. Apart from that, the condition number shows how much the boundary conditions can be changed due to a small error in the constant vector. Finally the null space of the solutions should always be one dimension other than the crossing point, which means ideally there's always only one zero singular value for the matrix. The uniqueness, ξ, defined by $\xi = \frac{\sigma_2}{\sigma_{min}}$, should be infinity all the time. To make the result more visible, $1/\kappa$ and $1/\xi$ are shown for the result.

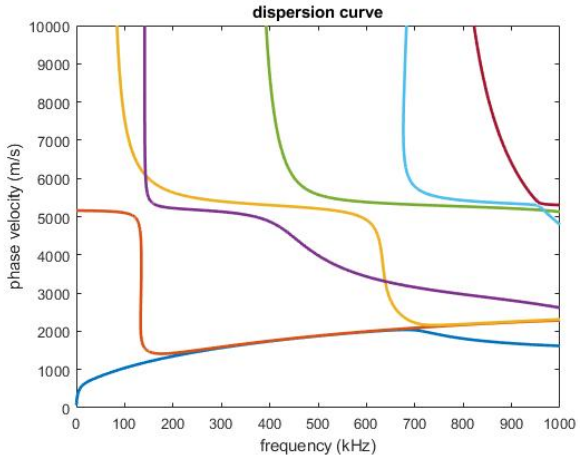

Figure 3-4 Sample Dispersion Curve for Sandwich Panel

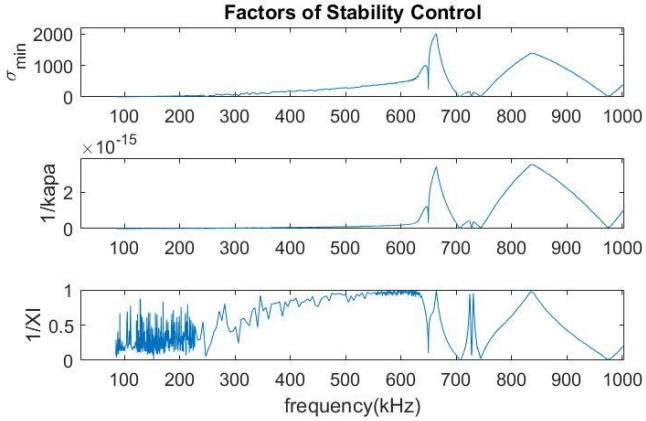

Figure 3-5 Sample Higher Mode Behavior of the Three Factors

Figure 3-5 shows the three-factor stability control for the first higher mode with cutoff frequency about 100 kHz. According to the σ_{min} frequency graph, generally speaking, the numerical error increases with the frequency. From 650kHz to 700 kHz, the result is extremely unstable. This is because at this frequency, the slope of the dispersion curve changes a lot, and with the root-finding algorithm, the numerical error can be a lot. At about 700 kHz to 750 kHz, the minimum singular value is small but 1/ ξ is very large. At this band, the mode is approach to another mode.

This results in a low uniqueness value. In conclusion, the three factors can predict about what type of numerical problem happened to the

3.3 Matrix form of the wave field

3.3.1 Obtaining the wave field by residue theorem and Jacobi's formula

Getting back to the time domain expression for assembling global matrix, as shown in the previous chapter:

$$\boldsymbol{GC}e^{i(kx-\omega t)} = 0 \tag{3-20}$$

In which $\boldsymbol{G}$ is the global matrix and $\boldsymbol{C}$ is the unknown constants. With the introduced forces applied on the boundary or interfaces, the expression (3-20) can be modulated to:

$$\boldsymbol{GC}e^{i(kx-\omega t)} = \boldsymbol{F}(x,t) = \boldsymbol{f}(t)\boldsymbol{g}(x) \tag{3-21}$$

$\boldsymbol{F}$ is a non-zero function vector indicating the forces applied on the boundary, which can be decomposed into a function vector about the time *t* multiplying another function vector about the space *x*. Applied 2D Fourier's transform to both side of the equation, one can obtain the frequency-wavenumber domain equation:

$$\boldsymbol{GC} = \widetilde{\boldsymbol{F}}(k,\omega) = \tilde{\boldsymbol{f}}(\omega)\widetilde{\boldsymbol{g}}(k) \tag{3-22}$$

The $\tilde{\boldsymbol{f}}(\omega)$ and $\widetilde{\boldsymbol{g}}(k)$ are the frequency and the wavenumber domain expression for $\boldsymbol{f}(t)$ and $\boldsymbol{g}(x)$. ω is the angular frequency and k is the angular wavenumber. So the problem can be solved in the frequency-wavenumber domain by the inverse of the GMM:

$$\boldsymbol{C} = \boldsymbol{G}^{-1}\widetilde{\boldsymbol{F}} = \frac{\boldsymbol{M}\widetilde{\boldsymbol{F}}}{\det(\boldsymbol{G})}$$

(3-23)

Where $\boldsymbol{M}$ is the adjoint matrix of $\boldsymbol{G}$ defined by:

$$M_{ji} = (-1)^{i+j} \det(G_{ij})$$

(3-24)

Where G_{ij} is $\boldsymbol{G}$ matrix without the ith row and jth column. Then apply the inverse Fourier's transform to equation (3-23) and be back to the frequency domain:

$$\boldsymbol{C} = \frac{1}{2\pi} \int_{-\infty}^{\infty} \frac{\boldsymbol{M}\widetilde{\boldsymbol{F}}}{\det(\boldsymbol{G})} e^{ikx} dk$$

(3-25)

Equation (3-25) shows the solution in frequency domain. Notice the poles of the expression satisfy the equation $\det(\boldsymbol{G}) = 0$, which is exactly the roots for dispersion equation shown in the previous chapter. A closed contour in the complex *k* plane with infinite radius was introduced to solve the integration.

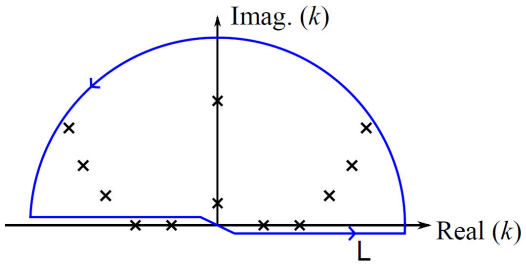

Figure 3-6: Closed Contour in the Upper Half Complex *k* Plane

Only positive real and imaginary *k* and the complex *k* with positive imaginary part are selected to ensure one direction propagation and convergence in the propagating direction. With this contour, one can obtain the infinite integration by applying residue theorem on equation (3-25) and get:

$$\boldsymbol{C} = \frac{1}{2\pi}(2\pi i)\left(\sum \frac{\boldsymbol{M}\widetilde{\boldsymbol{F}}}{\frac{\partial \det(\boldsymbol{G})}{\partial \mathrm{k}}}\right)e^{ikx}\Bigg|_{k=k_\alpha} = i\left(\sum \frac{\boldsymbol{M}\widetilde{\boldsymbol{F}}}{\frac{\partial \det(\boldsymbol{G})}{\partial \mathrm{k}}}\right)e^{ikx}\Bigg|_{k=k_\alpha}$$

(3-26)

Where k_α is the poles in the complex k domain. They also represent the roots for the dispersion equation, in another word, different modes, which are orthogonal to each other. With the Jocobi formula and the orthogonality of the modes, equation (3-26) can be further simplified to:

$$\boldsymbol{C}_\alpha = i\frac{\boldsymbol{M}\widetilde{\boldsymbol{F}}}{\frac{\partial \det(\boldsymbol{G})}{\partial \mathrm{k}}} = i\frac{\boldsymbol{M}\widetilde{\boldsymbol{F}}}{tr(\boldsymbol{M}\dot{\boldsymbol{G}})}$$

(3-27)

Where $\boldsymbol{C}_\alpha$ is the solution for mode α and $\dot{\boldsymbol{G}}$ is the derivative matrix for $\boldsymbol{G}$ with respect to k given as:

$$\dot{\boldsymbol{G}} = \begin{Bmatrix} \dot{\boldsymbol{Q}}_{21}(1) & \dot{\boldsymbol{Q}}_{22}(1)\boldsymbol{E}(1) + \boldsymbol{Q}_{22}(1)\dot{\boldsymbol{E}}(1) & \mathbf{0} & \mathbf{0} & \dots & \mathbf{0} & \mathbf{0} \\ \dot{\boldsymbol{Q}}_{11}(1)\boldsymbol{E}(1) + \boldsymbol{Q}_{11}(1)\dot{\boldsymbol{E}}(1) & \dot{\boldsymbol{Q}}_{12}(1) & -\dot{\boldsymbol{Q}}_{11}(2) & -\dot{\boldsymbol{Q}}_{12}(2)\boldsymbol{E}(2) + \boldsymbol{Q}_{12}(2)\dot{\boldsymbol{E}}(2) & \dots & \mathbf{0} & \mathbf{0} \\ \dot{\boldsymbol{Q}}_{21}(1)\boldsymbol{E}(1) + \boldsymbol{Q}_{21}(1)\dot{\boldsymbol{E}}(1) & \dot{\boldsymbol{Q}}_{22}(1) & -\dot{\boldsymbol{Q}}_{21}(2) & -\dot{\boldsymbol{Q}}_{22}(2)\boldsymbol{E}(2) + \boldsymbol{Q}_{22}(2)\dot{\boldsymbol{E}}(2) & \dots & \mathbf{0} & \mathbf{0} \\ \vdots & \vdots & \vdots & \vdots & \ddots & \vdots & \vdots \\ \mathbf{0} & \mathbf{0} & \mathbf{0} & \mathbf{0} & \dots & \dot{\boldsymbol{Q}}_{21}(N)\boldsymbol{E}(N) + \boldsymbol{Q}_{21}(N)\dot{\boldsymbol{E}}(N) & \dot{\boldsymbol{Q}}_{22}(N) \end{Bmatrix}$$

$$\dot{\mathbf{Q}}(\mathrm{m}) = \begin{bmatrix} i & \frac{k}{\eta_2} & k & -\frac{k}{\eta_2} \\ -\frac{k}{\eta_1} & i & \frac{k}{\eta_1} & i \\ -2i\frac{(k^2+\eta_1^2)}{\eta_1}\mu & -4k\mu & -2i\frac{(k^2+\eta_1^2)}{\eta_1}\mu & -4k\mu \\ 4k\mu & -2i\frac{(k^2+\eta_1^2)}{\eta_1}\mu & 4k\mu & 2i\frac{(k^2+\eta_1^2)}{\eta_1}\mu \end{bmatrix}$$

$$\dot{\mathbf{E}}(\mathrm{m}) = diag(-\frac{kh_m}{\eta_1}e^{-\eta_1 h_m} \quad -\frac{kh_m}{\eta_2}e^{-\eta_2 h_m})$$

(3-28)

The **Q** and **E** matrices are defined in the previous chapter. Finally, the displacement and stress vector in frequency domain can be express as:

$$\boldsymbol{U}(m) = \begin{Bmatrix} U \\ V \\ \Sigma_x \\ T \\ \Sigma_y \end{Bmatrix} = i\boldsymbol{Q}(m)\boldsymbol{E}(y,m)\ \frac{\boldsymbol{M}\widetilde{\boldsymbol{F}}}{tr(\boldsymbol{M}\dot{\boldsymbol{G}})}\, e^{ik_\alpha x} \tag{3-29}$$

Where $\boldsymbol{U}(m)$ is the displacement and stress vector in frequency domain for the mth layer. And $\boldsymbol{Q}(m)$ and $\boldsymbol{E}(y,m)$ have been defined in the previous chapter. Finally, by applying the inverse Fourier's transform in frequency domain, one can get back to the time domain solutions:

$$\boldsymbol{U}(t,m) = \int_{-\infty}^{\infty} i\boldsymbol{Q}(m)\boldsymbol{E}(y,m)\ \frac{\boldsymbol{M}\widetilde{\boldsymbol{F}}(\omega,k_\alpha)}{tr(\boldsymbol{M}\dot{\boldsymbol{G}})}\, e^{i(k_\alpha x-\omega t)} d\omega \tag{3-30}$$

Equation (3-30) shows the time response for any applied force on the boundary for a multi-layered medium.

3.3.2 Effects of the spatial distribution

The forcing function $\tilde{g}(k)$ can be obtained from Continues Fourier Transform (CFT). However, for most cases, it is hard to have the CFT for the spatial distribution function. Therefore, we are choosing the Discrete Fourier Transform (DFT) to simulate the spatial distribution function in a limited region. To study the convergence of DFT to CFT specific on lamb wave excitation, the signal used in this thesis is a uniform square loading with 10mm loading diameter. Or the spatial distribution function can also be represented by the piecewise continues function:

$$g(x) = \begin{cases} 1 & -0.005 \le x \le 0.005 \\ 0 & otherwise \end{cases} \tag{3-31}$$

The CFT of this function can be expressed by:

$$\tilde{g}(k) = \frac{2\sin(0.005k)}{k}$$

(3-32)

To compute the DFT, the algorithm fast Fourier transform(FFT) is applied. The algorithm can be expressed by the formula:

$$X_k = \sum_{n=0}^{N-1} x_n e^{-\frac{i2\pi k_n}{N}} \qquad k = 0, 1, \ldots N-1$$

(3-33)

The result from the two method are compared with a special increment $\Delta x = 0.05\ mm$ and 20000 sampling points.

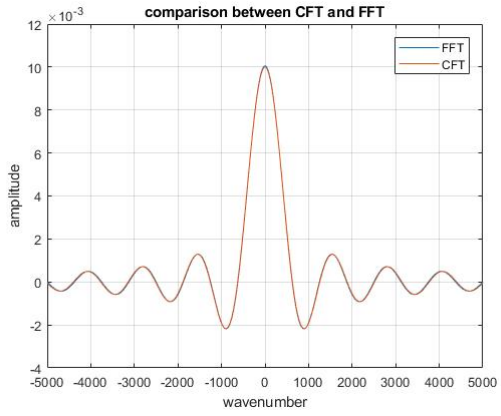

Figure 3-7 Comparison Between CFT and FFT

It can be seemed that the setting within $-5000 < k < 5000$ converges well. With this setting, the spatial response from a transducer is simulated by a gaussian windowed function with L = 10mm and α = 3.5. The function can be expressed by:

$$w(n) = e^{-\frac{1}{2}\left(\alpha\frac{2n}{(L-1)}\right)^2}$$

(3-34)

The function has a square window between x = -5mm and x = 5mm. The distribution is shown in Figure 3-8.

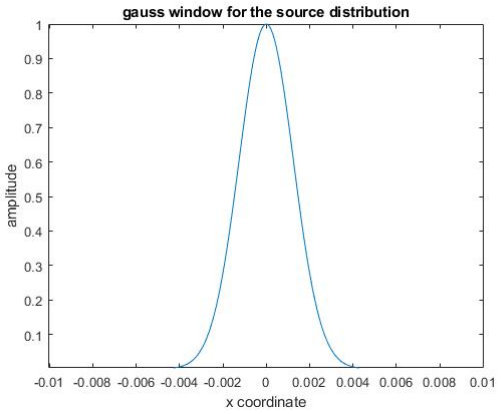

Figure 3-8 Spatial Distribution of the Source

3.3.3 Band filter applied to the response

With the spatial distribution given in the previous chapter and 200kHz 5 cycles Hann windowed temporal distribution, the response of a 2mm aluminum plate under the vertical loading can be calculated by equation (3-30).

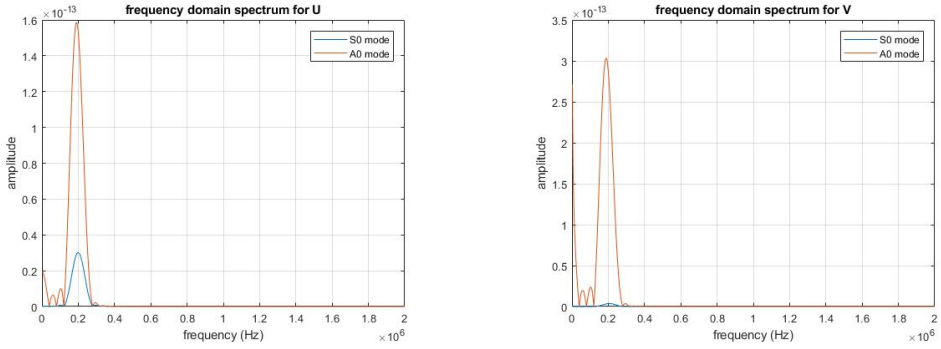

Figure 3-9 The Response of Vertical Loading with Temporal and Spatial Distribution

Figure 3-9 shows that the response has a singularity point when the frequency $\omega = 0$. This is true since wave equation only works when the frequency or wavenumber is large enough so that

the media can be considered as infinity. However, in real experiment, since the devices including the transducers and amplifier have build-in filters, the low frequency effect will not be shown in experimental results. To avoid the low frequency effect, a bandpass 4th order Bessel filter from 20kHz to 1MHz is applied to the solution. To compare the two cases, the displacements at the surface with 500 mm distance from the source are calculated.

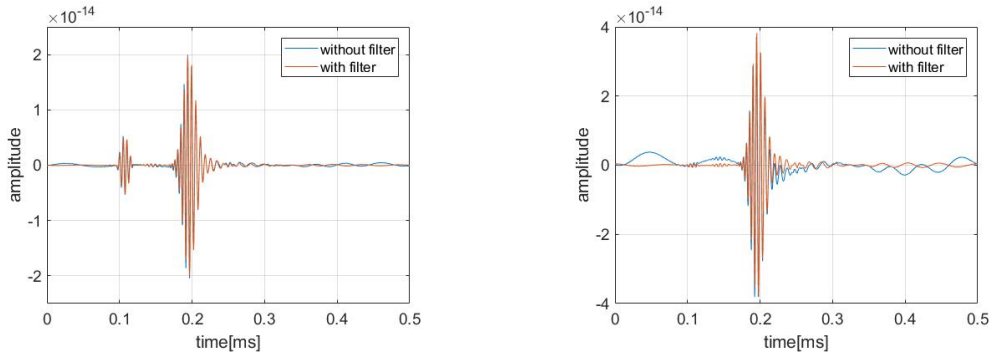

Figure 3-10 Comparison between the cases with/without the filter for (a) horizontal displacement and (b) vertical displacement

With the bandpass filter, both the horizontal displacement and vertical displacement can be improved, while the vertical displacement improved more.

3.4 Singularities in the dispersion equations

3.4.1 Numerical issues in the original dispersion equations

During studying the frequency domain response of a plate, a numerical issue is found in the response. At certain frequencies in certain mode, the response of the plate becomes “unstable” with a large variation. For example, with a broadband concentrated excitation, the S_0 mode responses in a 4mm aluminum plate can be show in the following figures:

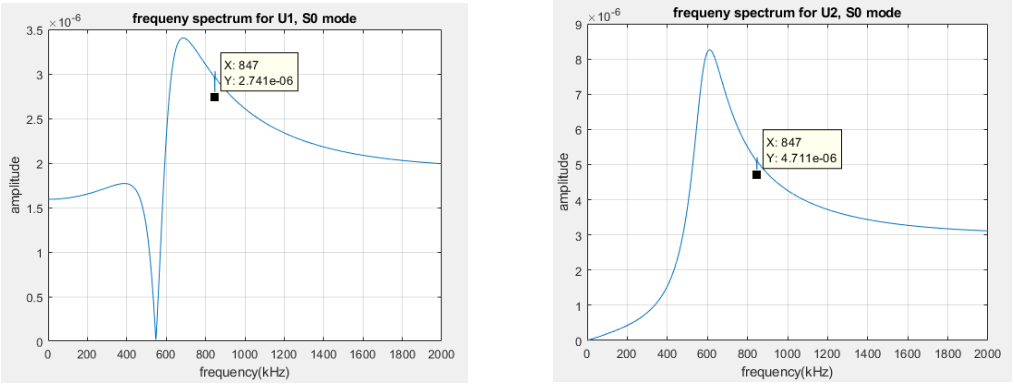

Figure 3-11 S_0 mode surface responses of 4mm aluminum plate in (a) horizontal displacement and (b) vertical displacement

Figure 3-11 show the singular points happens when the frequency $\omega = 847$ kHz or $\Omega = 3.39$ MHz. At this frequency, the relation $\eta_2 = \sqrt{k^2 - k_2^2} = 0$ can be obtained, which indicates the wavenumber coefficient η_2 turns from a real number to an imaginary number. At this location, the complex modes cross with the real modes and forms a singularity point on the dispersion curves. In equation (3-27), both the numerator and the denominator at this point equals to zero, and therefore numerically the solution will have trouble dealing with this formula, creating a "0/0" type numerical error.

3.4.2 Modified formulas to avoid the numerical issue

To avoid this error, the singular points are removed from the equation (3-23) by dividing η_1 and η_2 for both the numerator and the denominator, and take the inverse Fourier transform to the normalized equation. The modified equation of (3-23) can be written as:

$$\boldsymbol{C} = \boldsymbol{G}^{-1}\widetilde{\boldsymbol{F}} = \frac{\dfrac{\boldsymbol{M}\widetilde{\boldsymbol{F}}}{\prod \eta_i}}{\dfrac{\det(\boldsymbol{G})}{\prod \eta_i}} \tag{3-35}$$

And after taking the inverse Fourier transform, the expression (3-29) can be rewritten as:

$$\boldsymbol{U}(m) = i\boldsymbol{Q}(m)\boldsymbol{E}(y,m)\ \frac{\dfrac{\boldsymbol{M}\widetilde{\boldsymbol{F}}}{\prod \eta_i}}{\dfrac{tr\left(\boldsymbol{M}\dot{\boldsymbol{G}}\right)}{\prod \eta_i} - \dfrac{\det(\boldsymbol{G})\dfrac{\partial(\prod \eta_i)}{\partial k}}{\prod \eta_i^2}}\, e^{ik_\alpha x}$$

(3-36)

Since $\eta_i = \sqrt{k^2 - k_i^2}$ and k_i is independent to k, the derivative in (3-36) can be calculated by:

$$\frac{\partial(\prod \eta_i)}{\partial k} = \sum \frac{k}{\eta_i} \prod_{j \neq i} \eta_j = \sum \frac{k}{\eta_i^2} \prod \eta_j$$

$$\boldsymbol{U}(m) = i\boldsymbol{Q}(m)\boldsymbol{E}(y,m)\ \frac{\dfrac{\boldsymbol{M}\widetilde{\boldsymbol{F}}}{\prod \eta_i}}{\dfrac{tr\left(\boldsymbol{M}\dot{\boldsymbol{G}}\right)}{\prod \eta_i} - \dfrac{k\det(\boldsymbol{G})\sum \dfrac{1}{\eta_i^2}}{\prod \eta_i}}\, e^{ik_\alpha x}$$

$$= i\boldsymbol{Q}(m)\boldsymbol{E}(y,m)\ \frac{\boldsymbol{M}\widetilde{\boldsymbol{F}}}{tr\left(\boldsymbol{M}\dot{\boldsymbol{G}}\right) - k\det(\boldsymbol{G})\sum \dfrac{1}{\eta_i^2}}\, e^{ik_\alpha x}$$

$$= i\boldsymbol{Q}(m)\boldsymbol{E}(y,m)\ \frac{\boldsymbol{M}\widetilde{\boldsymbol{F}}\prod \eta_i^2}{tr\left(\boldsymbol{M}\dot{\boldsymbol{G}}\right)\prod \eta_i^2 - k\det(\boldsymbol{G})\sum_i \prod_{i \neq j} \eta_j^2}$$

(3-37)

With equation (3-37), the numerical instability will be removed. It can be seen that the numerical instability is created by the numerical error in $\det(\boldsymbol{G})$, which is canceled by the second term in the denominator.

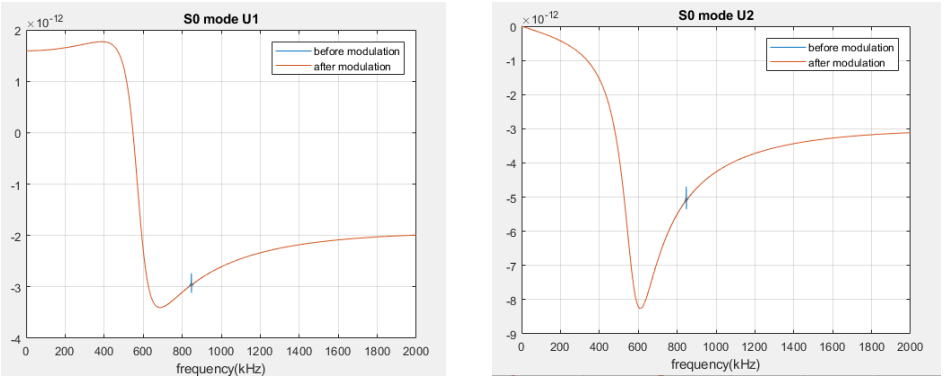

Figure 3-12 Comparison between the solution before and after modification for (a) horizontal displacement and (b) vertical displacement for S_0 mode

The improved formular helps in predicting the solution not only in the frequency domain but also in the time domain. The residue signal is close to a single-frequency signal in the time domain, which will create uncertainty in NDE especially when dealing with case that is sensitive to the phase change. An example is shown below with a excitation of 850kHz in a 4mm plate. The residue signal is calculated by:

$$y_{residue} = \frac{y_a - y_b}{\max(|y_a|)} \times 100\% \tag{3-38}$$

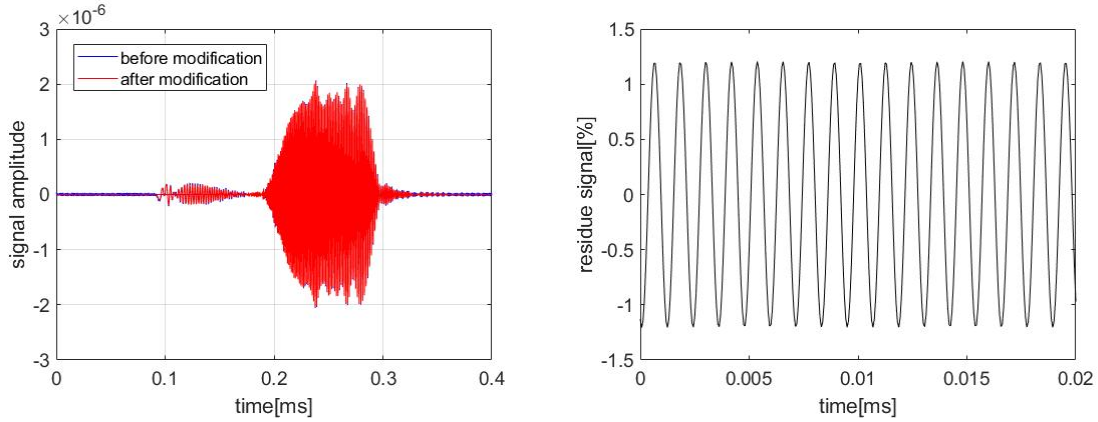

Figure 3-13 (a) Comparison between the two solutions (b) residue signal in percentage

3.5 In influence of the core properties on the dispersion curves of a sandwich structure

3.5.1 Homogenized honeycomb core properties

Consider a composite layer as shown in Figure 3-14 where we define a global stiffness matrix in which the x_1-axis and x_2-axis lies in the plane of the material layer and x_3-axis along the thickness of the layer.

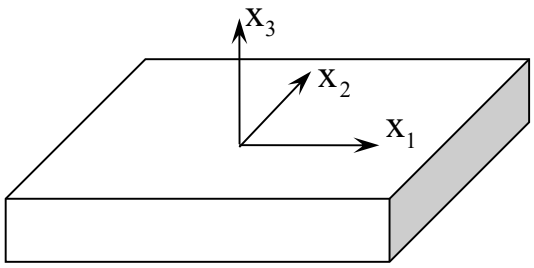

Figure 3-14 Model of a composite layer

For a homogeneous and transversely isotropic material with 1-2 plane be the special plane of isotropy the stress can be expressed linearly in terms of the displacement by the following stress-displacement relations:

$$\begin{Bmatrix}\sigma_{11}\\ \sigma_{22}\\ \sigma_{33}\\ \sigma_{23}\\ \sigma_{31}\\ \sigma_{12}\end{Bmatrix} = \begin{bmatrix} C_{11} & C_{12} & C_{13} & 0 & 0 & 0 \\ C_{12} & C_{11} & C_{13} & 0 & 0 & 0 \\ C_{13} & C_{13} & C_{33} & 0 & 0 & 0 \\ 0 & 0 & 0 & C_{44} & 0 & 0 \\ 0 & 0 & 0 & 0 & C_{44} & 0 \\ 0 & 0 & 0 & 0 & 0 & \frac{1}{2}(C_{11}-C_{12}) \end{bmatrix} \begin{Bmatrix} u_{1,1}\\ u_{2,2}\\ u_{3,3}\\ u_{2,3}+u_{3,2}\\ u_{1,3}+u_{3,1}\\ u_{1,2}+u_{2,1}\end{Bmatrix} \tag{3-39}$$

With a general form of the solution:

$$u = Ae^{i(kx-\omega t)+\eta z} \qquad w = Be^{i(kx-\omega t)+\eta z}$$

(3-40)

The equations of motions can be expressed by:

$$\left(\frac{C_{44}\eta^2 - C_{11}k^2}{\rho} + \omega^2\right)A + \left(\frac{(C_{13}+C_{44})ik\eta}{\rho}\right)B = 0$$

$$\left(\frac{(C_{13}+C_{44})ik\eta}{\rho}\right)A - \left(\frac{C_{44}k^2 - C_{33}\eta^2}{\rho} - \omega^2\right)B = 0$$

(3-41)

To simplify the equation (3-41), four constants are defined:

$$c_1^2 = \frac{C_{11}}{\rho} \qquad c_2^2 = \frac{C_{55}}{\rho} \qquad c_3^2 = \frac{C_{33}}{\rho} \qquad c_4^2 = \frac{C_{13}+C_{55}}{\rho}$$

(3-42)

All four constants are defined by the material stiffness and the density, and all of them are in units of velocity. The first three constants c_1, c_2 and c_3 are the three Bulk waves velocities of the transversely isotropic material. With the four constants, (3-41) can be further simplified to:

$$(c_2^2\eta^2 - c_1^2k^2 + \omega^2)A + (c_4^2ik\eta)B = 0$$

$$(c_4^2ik\eta)A - (c_2^2k^2 - c_3^2\eta^2 - \omega^2)B = 0$$

(3-43)

For a non-trivial solution set of A and B, the coefficients of equation (3-43) must satisfied the condition:

$$\left(\frac{\eta^2}{k_2^2} - \frac{\eta_1^2}{k_1^2}\right)\left(\frac{\eta^2}{k_3^2} - \frac{\eta_2^2}{k_2^2}\right) + \frac{k^2\eta^2}{k_4^4} = 0$$

(3-44)

Where

$$k_j^2 = \frac{\omega^2}{c_j^2} \qquad \eta_j^2 = k^2 - k_j^2$$

Now define

$$\eta_\alpha^2 = \frac{\eta_1^2 k_2^2}{k_1^2} \qquad \eta_\beta^2 = \frac{\eta_2^2 k_3^2}{k_2^2} \qquad \eta_\gamma^2 = \frac{k^2 k_2^2 k_3^2}{k_4^4}$$

The condition (3-44) can be rewrite to:

$$\eta^4 + \left(-\eta_\alpha^2 - \eta_\beta^2 + \eta_\gamma^2\right)\eta^2 + \eta_\alpha^2 \eta_\beta^2 = 0 \tag{3-45}$$

Equation (3-45) is a quadratic equation of η^2. The roots of the equation can be calculated analytically with

$$\eta^2 = \frac{1}{2}\left(-\bar{B} \pm \sqrt{\bar{B}^2 - 4\bar{C}}\right) \tag{3-46}$$

Where $\bar{B}$ is the coefficient of η^2 term and $\bar{C}$ is the coefficient of 1. The term $\bar{B}^2 - 4\bar{C}$ can be simplified with following calculation process:

$$\begin{aligned}
\bar{B}^2 - 4\bar{C} &= \left(\eta_\beta^2 + \eta_\alpha^2\right)^2 - 2\eta_\gamma^2\left(\eta_\alpha^2 + \eta_\beta^2\right) + \eta_\gamma^4 - 4\eta_\alpha^2\eta_\beta^2 \\
&= \left(\eta_\alpha^2 - \eta_\beta^2\right)^2 - 2\eta_\gamma^2\left(\eta_\alpha^2 + \eta_\beta^2\right) + \eta_\gamma^4 \\
&= \left(\eta_\alpha^2 - \eta_\beta^2\right)^2 - 2\left(\eta_\alpha^2 - \eta_\beta^2\right)\eta_\gamma^2 - 4\eta_\gamma^2\eta_\beta^2 + \eta_\gamma^4 \\
&= \left(\eta_\alpha^2 - \eta_\beta^2 - \eta_\gamma^2\right)^2 - 4\eta_\gamma^2\eta_\beta^2 \\
&= \left[\left(\eta_\alpha^2 - \eta_\beta^2 - \eta_\gamma^2\right) + 2\eta_\gamma\eta_\beta\right]\left[\left(\eta_\alpha^2 - \eta_\beta^2 - \eta_\gamma^2\right) - 2\eta_\gamma\eta_\beta\right] \\
&= \left[\eta_\alpha^2 - \left(\eta_\beta - \eta_\gamma\right)^2\right]\left[\eta_\alpha^2 - \left(\eta_\beta + \eta_\gamma\right)^2\right] \\
&= (\eta_\alpha + \eta_\beta - \eta_\gamma)(\eta_\alpha - \eta_\beta + \eta_\gamma)(\eta_\alpha - \eta_\beta - \eta_\gamma)(\eta_\alpha + \eta_\beta + \eta_\gamma)
\end{aligned} \tag{3-47}$$

So the solution of (3-46) can be expressed by:

$$\eta^2 = \frac{1}{2}\left[\left(\eta_\alpha^2 + \eta_\beta^2 - \eta_\gamma^2\right) \pm \sqrt{\left(\eta_\alpha + \eta_\beta - \eta_\gamma\right)\left(\eta_\alpha - \eta_\beta + \eta_\gamma\right)\left(\eta_\alpha - \eta_\beta - \eta_\gamma\right)\left(\eta_\alpha + \eta_\beta + \eta_\gamma\right)}\right]$$

(3-48)

According to equation (3-48), there are four solutions of η. These four solutions will be expressed as η_n and η_m in the following part of the theses. Next, two variables R_n and R_m are defined by:

$$R_n = \frac{B_n}{A_n} = \frac{ik\eta_n}{\left(\frac{k^2}{k_2^2} - \frac{\eta_n^2}{k_3^2} - 1\right)k_4^2} \qquad R_m = \frac{B_m}{A_m} = \frac{ik\eta_m}{\left(\frac{k^2}{k_2^2} - \frac{\eta_m^2}{k_3^2} - 1\right)k_4^2}$$

(3-49)

And the displacements can be written as:

$$U = (\bar{A}\cosh(\eta_n y) + \bar{B}\sinh(\eta_n y) + \bar{C}\cosh(\eta_m y) + \bar{D}\sinh(\eta_m y))e^{ikx}$$

$$W = (\bar{A}R_n\sinh(\eta_n y) + \bar{B}R_n\cosh(\eta_n y) + \bar{C}R_m\sinh(\eta_m y) + \bar{D}R_m\cosh(\eta_m y))e^{ikx}$$

Where

$$\bar{A} = \frac{A+B}{2} \quad \bar{B} = \frac{A-B}{2} \quad \bar{C} = \frac{C+D}{2} \quad \bar{D} = \frac{C-D}{2}$$

(3-50)

By substituting the solution (3-50) into boundary conditions given in equation (3-51), the dispersion equation can be expressed as:

$$y = \pm H, \qquad \sigma_{zz} = \tau_{xz} = 0$$

(3-51)

$$\frac{\tanh(\eta_n H)}{\tanh(\eta_m H)} = \frac{(ik\zeta_{13} + \eta_n R_n \zeta_{33})(\eta_m + ikR_m)}{(ik\zeta_{13} + \eta_m R_m \zeta_{33})(\eta_n + ikR_n)}$$

for the symmetric case and

$$\frac{\tanh(\eta_m H)}{\tanh(\eta_n H)} = \frac{(ik\zeta_{13} + \eta_n R_n \zeta_{33})(\eta_m + ikR_m)}{(ik\zeta_{13} + \eta_m R_m \zeta_{33})(\eta_n + ikR_n)} \tag{3-52}$$

for the antisymmetric case. In which,

$$\zeta_{13} = \frac{C_{13}}{C_{44}} = \frac{k_2^2}{k_4^2} - 1 \qquad \zeta_{33} = \frac{C_{33}}{C_{44}} = \frac{k_2^2}{k_3^2} \tag{3-53}$$

Considering a three-layer symmetric composite structure, by applying a symmetric or antisymmetric boundary condition, the global matrix for a three-layer composite can be expressed by:

$$Q(m)_{1-4,1-4} = \begin{bmatrix} \zeta_m & \zeta_n & \zeta_m & \zeta_n \\ -ik\eta_m k_3^2 & -ik\eta_n k_3^2 & ik\eta_m k_3^2 & ik\eta_n k_3^2 \\ -C_{44}\eta_m(\zeta_m - k^2 k_3^2) & -C_{44}\eta_n(\zeta_n - k^2 k_3^2) & C_{44}\eta_m(\zeta_m - k^2 k_3^2) & C_{44}\eta_n(\zeta_n - k^2 k_3^2) \\ C_{13}ik\zeta_m + C_{33}ik\eta_m^2 k_3^2 & C_{13}ik\zeta_n + C_{33}ik\eta_n^2 k_3^2 & C_{13}ik\zeta_m + C_{33}ik\eta_m^2 k_3^2 & C_{13}ik\zeta_n + C_{33}ik\eta_n^2 k_3^2 \end{bmatrix}$$

$$E(m) = \begin{bmatrix} e^{-\eta_m H} & 0 \\ 0 & e^{-\eta_n H} \end{bmatrix}$$

$$GS = \begin{bmatrix} Q(1)_{34,12} & Q(1)_{34,34}E(1) & \mathbf{0} & \mathbf{0} \\ Q(1)_{12,12}E(1) & Q(1)_{12,34} & -Q(2)_{12,12} & -Q(2)_{12,34}E(2) \\ Q(1)_{34,12}E(1) & Q(1)_{34,34} & -Q(2)_{34,12} & -Q(2)_{34,34}E(2) \\ \mathbf{0} & \mathbf{0} & Q(2)_{23,12}E(2) & Q(2)_{23,34} \end{bmatrix}$$

$$GA = \begin{bmatrix} Q(1)_{34,12} & Q(1)_{34,34}E(1) & \mathbf{0} & \mathbf{0} \\ Q(1)_{12,12}E(1) & Q(1)_{12,34} & -Q(2)_{12,12} & -Q(2)_{12,34}E(2) \\ Q(1)_{34,12}E(1) & Q(1)_{34,34} & -Q(2)_{34,12} & -Q(2)_{34,34}E(2) \\ \mathbf{0} & \mathbf{0} & Q(2)_{14,12}E(2) & Q(2)_{14,34} \end{bmatrix} \tag{3-54}$$

By using the searching method above, the solution for the composite sandwich panel can be computed and more studies can be done on sandwich composite.

3.5.2 Features of guided waves propagating in a honeycomb sandwich structure

Consider an HSS with CFRP face sheets (1.78 mm, quasi-isotropic stacking sequence) and an aluminum honeycomb core (12.7 mm), as shown in the Figure 3-15. To simplify the modeling of the HSS and compute the dispersion curves easily, a homogenized three-layer model is used. The homogenized transversely isotropic material properties of both the face sheets and the core layer are computed based on mixture theories [27, 28]. The determined nominal values are summarized in Table 3-1. It should be noted that the 1- and 2-axes represent the in-plane directions, and the 3-axis points along the out of plane direction.

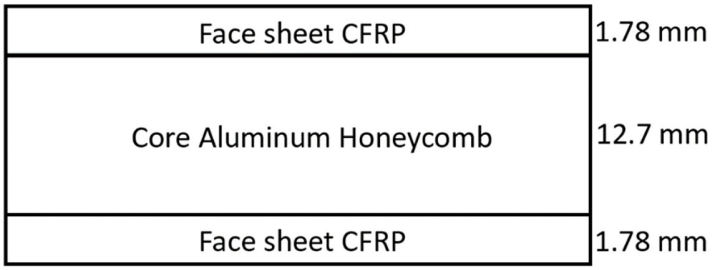

Figure 3-15 Dimensions of the homogenized HSS model

	E_1	E_3	ν_{12}	ν_{13}	G_{13}	ρ
Skin	38.8	9.8	0.31	0.32	2.9	1276
Core	3.43e-3	2.99	0.999	3.79e-4	0.413	114.4

Table 3-1 Homogenized material properties: elastic moduli in [GPa] and densities in [kg/m^3]

The stiffness matrix for any orthotropic material needs to be positive-definite to guarantee that the strain energy is positive. In other words, the material properties should satisfy, among others, the following constraints:

$$|\nu_{ij}| < \sqrt{\frac{E_i}{E_j}}$$

$$\overline{\Delta} = 1 - \nu_{12}\nu_{21} - \nu_{23}\nu_{32} - \nu_{13}\nu_{31} - 2\nu_{21}\nu_{32}\nu_{13} > 0$$

(3-55)

A sensitivity study is performed to evaluate the influence of the material constants of the honeycomb core on the guided wave characteristics for the HSS. The assumed uncertainty interval of the five constants of the assumed transversely isotropic core layer are summarized in Table 3-2. In each of the following studies, only one parameter is varied at a time while the others are kept constant.

	Lower Bound	Upper Bound	Step
E_1[MPa]	30	400	10
E_3[GPa]	2.5	3.5	0.1
ν_{12}	0.95	0.9999	log.
ν_{13}	1e-5	4e-4	4e-5
G_{13}[MPa]	350	450	10

Table 3-2 Considered variations in material properties for core layer

Figure 3-16 shows the influence of E_1, E_3, ν_{13} and G_{13} of the core layer on the group velocities of the two fundamental modes. The following observations can be made:

1. Young's modulus E_1 changes is varied by approximately 30% of its nominal value. However, only the $S0$ mode seems to be affected, predominantly in the region below 50kHz, as shown in Figure 3-16 a). The maximum variation is approximately 3.6% of the group velocity at 5kHz.
2. Young's modulus E_3 is also varied by approximately 30%. Similar to E_1, E_3 mainly affects the $S0$ mode, as shown in Figure 3-16 b). The majorly of the affected region is, however, slightly higher at around 50-100kHz.
3. Poisson's ratio ν_{13} is varied within the bounds discussed. As can be seen from Figure 3-16 c), again only the $S0$ mode is affected. Significant changes occur in the range from approximately 25kHz to 100kHz.

4. Shear modulus G_{13} is also varied by approximately 30% of its nominal value. Unlike the other three material properties, G_{13} only substantially affects the $A0$ mode. At the same time, the changes in the group velocity are comparably small with a maximum deviation of approximately 15% at 5kHz.
5. Common across all four cases, the convergence velocity of neither of the fundamental modes is affected by a variation of these parameters within the given bounds.

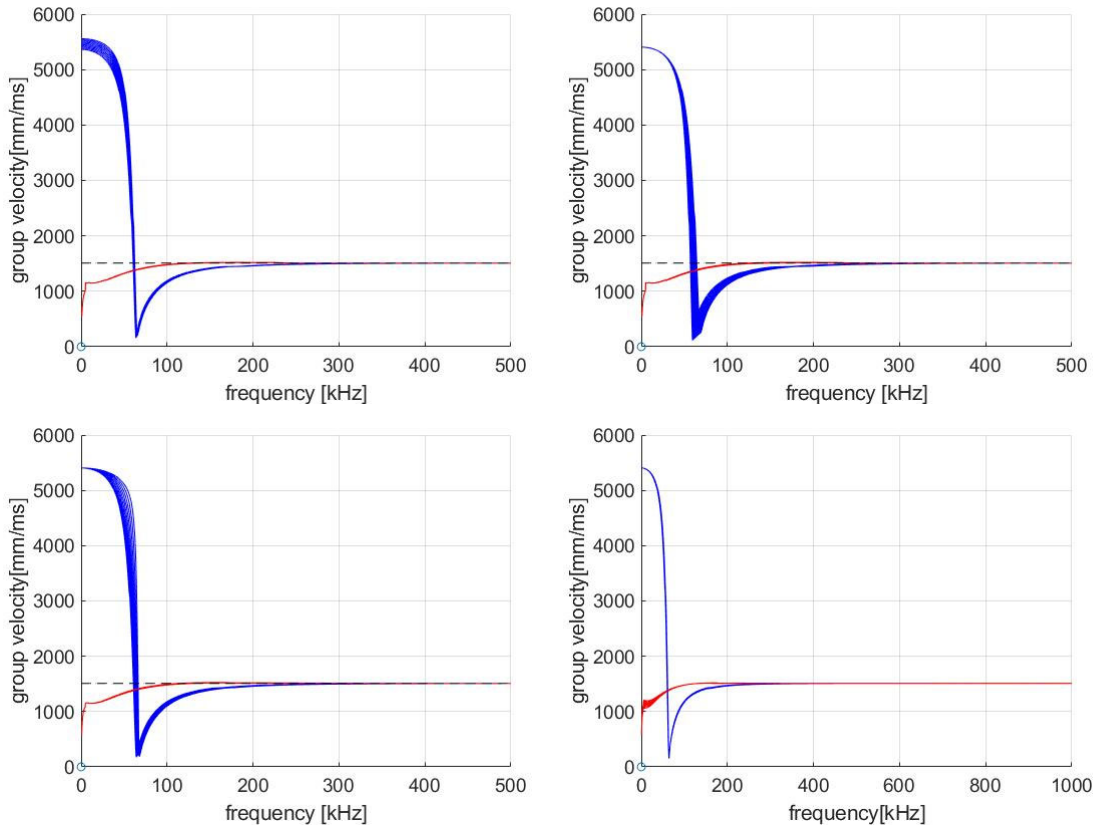

Figure 3-16 Group velocities of the fundamental modes for varying core material properties: a) for E_1 b) for E_3 c) a) for ν_{13} d) for G_{13}

It should be noted that Poisson's ratio ν_{12} is calculated to be $\nu_{12} = 1$ based on mixture theory. However, this is in violation of the constraint from (3-55). Thus, in previous publications [29]

[30] a value of $\nu_{12} = 0.999$ had been assumed. As shown in the following, this rather arbitrary assumption may lead to incorrect calculation of the dispersion curves.

To begin the discussion, the dispersion curves are calculated for $\nu_{12} = 0.95$ and the results are shown in Figure 3-17.

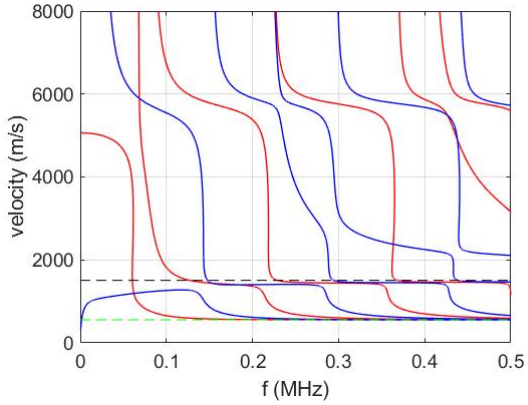

Figure 3-17 Dispersion curves and convergence velocities for $\nu_{12} = 0.95$

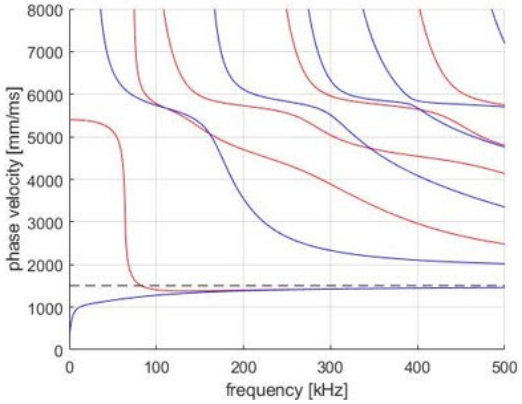

Figure 3-18 Dispersion curves for the HSS with nominal material properties

First it should be noted that a deviation of only approximately 5% from the nominal value for ν_{12} leads to substantial differences. To highlight these effects, the longitudinal bulk velocity c_1 of the

homogenized core layer is shown as a green dashed line in addition to the black dashed line representing the Rayleigh wave velocity c_R of the face sheet material. As can be seen from the figure, now the velocities for all modes only "converge" towards the Rayleigh wave velocity for a short frequency range before finally converging towards the longitudinal bulk velocity.

This trend can be further visualized by artificially combining all modes within their "short-range" convergence region, as shown as a black line in Figure 3-17. The trend that highlighted is very close to the $A0$ mode of the case that $\nu_{12} = 0.999$, and is one of the main targets for the following research.

In a next step, the value of ν_{12} is slowly increased from 0.95 to its nominal value of 0.999, and its effects on the group velocities of the fundamental modes is analyzed. The results are shown in Figure 3-19.

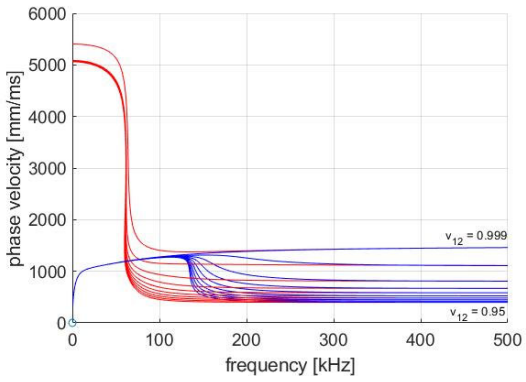

Figure 3-19 Phase velocity of the fundamental modes for varied values of ν_{12}

As compared to all other material constants, significantly different trends can be observed. In particular, the convergence velocity significantly changes with changes in ν_{12}. Most importantly, for most values of ν_{12} a substantial drop in velocity occurs after intermittently converging

towards c_R. For a comparison between the results for the extreme values and their effects on all modes.

In summary, from Figure 3-19, it can be seen that ν_{12} strongly affects the pattern of the dispersion curves for an HSS. In fact, a critical point is reached when c_1 of the core is equal to the c_R of the face sheet. The critical point is visualized in Figure 3-20, showing the dependence of the bulk velocities [31] on the value of ν_{12} of the homogenized core.

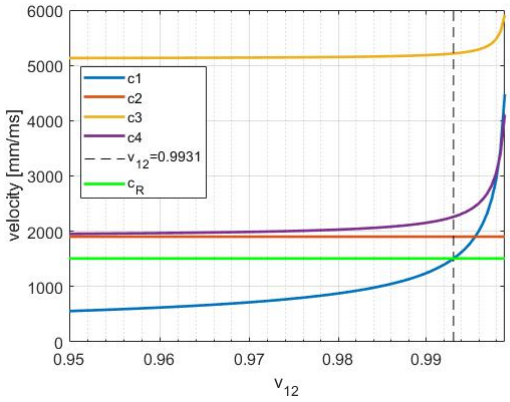

Figure 3-20 Bulk waves velocities of the core for different values of ν_{12}

By inspection, it can be seen that $c_1 = c_R$ at $\nu_{12} = 0.9931$. In other words, when $\nu_{12} < 0.9931$, the dispersion curves show an intermittent pseudo-convergence behavior towards c_R of the face sheet while ultimately converging towards c_1 of the core, while for $\nu_{12} > 0.9931$, the dispersion curves directly converge towards c_R of the face sheet as shown in Figure 3-18.

3.6 A model of lamb wave damping

3.6.1 Q-factor based damping model

In 1964, experiment observed that for an isotropic solid, following conclusions can be dropped [32]:

1. $\hat{\alpha}, \hat{\beta}, Q_\alpha, Q_\beta$ are independent of frequency in a broad frequency range.
2. Where $\hat{\alpha}, \hat{\beta}$ are the Bulk wave velocity and Q_α, Q_β are the quality factor.
3. Q_α, Q_β are proportional to the wave speeds $\hat{\alpha}, \hat{\beta}$.
4. The numerical values of Q_α, Q_β are very large (>100).

Where $\hat{\alpha}$ is the velocity of longitudinal Bulk wave while $\hat{\beta}$ is the velocity of shear Bulk wave. Q_α and Q_β are the corresponding quality factors and are defined by:

$$Q = \frac{\hat{k}}{2k_{imag}} \tag{3-56}$$

Where $\hat{k}$ is the real wave number and k_{imag} is the imaginary wave number that leads to the decaying of the waves. Based on the observations that $Q \propto \hat{c}$, one can drop the conclusions that

$$2Q_\beta = \frac{\hat{k}}{k_{imag}} \propto \hat{\beta} = c\hat{\beta} > 200$$

$$k_{imag} = \frac{\hat{k}}{2Q_\beta} \tag{3-57}$$

Where c is a constant that shows the proportionality of the Q_β with respect to the shear wave velocity $\hat{\beta}$. Calculation can be done to relate the shear modulus with the constant:

$$\frac{\mu_{complex}}{\rho} = \beta^2 = \frac{\omega^2}{k^2}$$

$$k^2 = \left(\hat{k} + ik_{imag}\right)^2 = \hat{k}^2\left(1 + i\frac{1}{2Q_\beta}\right)^2 = \hat{k}^2\left(1 + i\frac{1}{2Q_\beta} - \frac{1}{4Q_\beta^2}\right)$$

$$\approx \hat{k}^2\left(1 + i\frac{1}{2Q_\beta}\right) = \hat{k}^2(1 + ip)$$

$$\mu_{complex} = \frac{\hat{\mu}}{1 + ip}$$

(3-58)

Where $p = \frac{1}{2Q_\beta}$.

From (3-58), if we assume that the proportional ratio c remains constants for the same material, the Q factor related to the longitudinal wave can be expressed as:

$$2Q_\alpha = 2Q_\beta \frac{\hat{\alpha}}{\hat{\beta}}$$

And therefore:

$$\lambda_{complex} + 2\mu_{complex} = \frac{\hat{\lambda} + 2\hat{\mu}}{1 + ip\frac{\hat{\beta}}{\hat{\alpha}}}$$

(3-59)

These results can be applied to a transversely isotropic solid with four independent Bulk waves velocities [33]. With a stiffness matrix given by (3-39), the complex stiffness can be expressed by:

$$C_{11} = \frac{\widehat{C_{11}}}{1 + ip\sqrt{\frac{\widehat{C_{44}}}{\widehat{C_{11}}}}}$$

$$C_{33} = \frac{\widehat{C_{33}}}{1 + ip\sqrt{\frac{\widehat{C_{44}}}{\widehat{C_{33}}}}}$$

$$C_{44} = \frac{\widehat{C_{44}}}{1 + ip}$$

$$C_{13} = \frac{\widehat{C_{13}} + \widehat{C_{44}}}{1 + ip\sqrt{\frac{\widehat{C_{44}}}{\widehat{C_{13}} + \widehat{C_{44}}}}} - C_{44}$$

(3-60)

To obtain the imaginary part of the root, Newton's iteration is used.

$$k_{n+1} = k_n - \frac{f(k_n)\Delta k}{f(k_n + \Delta k) - f(k_n)}$$

(3-61)

3.6.2 Experimental validation of the damping model

To validate the damping factor, both the spreading effect and Q-factor damping are considered. Similar to the well-known inverse square law, the intensity for the Lamb wave follows the inverse law since Lamb wave has a 2D circular wave front, as shown in Figure 3-21.

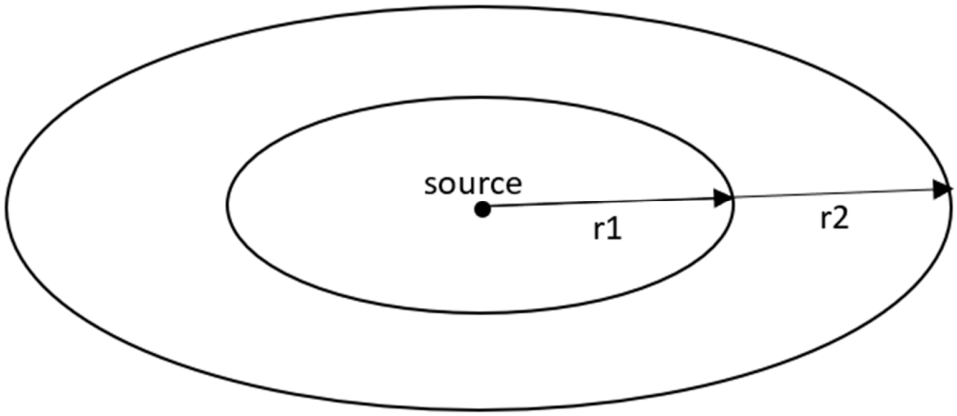

Figure 3-21 Energy dissipation due to spreading effect

The amplitude of the signal is inversely proportional to the square-root of the propagating distance. Besides, as stated in the previous subchapter, the q factor has an exponentially decaying effect to the amplitude of signal. Therefore, the amplitude of the signal can be expressed by the formula:

$$\mathrm{A(x)} = \frac{A_0}{\sqrt{x - x_0}} e^{-\alpha(x - x_0)} \tag{3-62}$$

A_0 is the initial amplitude of the signal and x_0 is the starting location where the wave forms. By taking the logarithm of (3-62), and substituting $x = x_1, x_2, x_3$ ... which is the distance between the source and the receiver measured in experiment, (3-62) becomes an optimization problem:

Find x_0

Minimize $\|\boldsymbol{Ac} - \boldsymbol{y}\|_2$

Subject to $\boldsymbol{c} = (\boldsymbol{A}^T\boldsymbol{A})^{-1}\boldsymbol{A}^T\boldsymbol{y}$ (least square fit)

Where:

$$\boldsymbol{A} = \begin{bmatrix} -(x_1 - x_0) & 1 \\ -(x_2 - x_0) & 1 \\ \vdots & \vdots \\ -(x_n - x_0) & 1 \end{bmatrix} \quad \mathbf{c} = \begin{bmatrix} \alpha \\ -\ln(A_0) \end{bmatrix} \quad \mathbf{y} = \begin{bmatrix} \ln(A(x_1) + 0.5\ln(x_1 - x_0) \\ \ln(A(x_1) + 0.5\ln(x_2 - x_0) \\ \vdots \\ \ln(A(x_1) + 0.5\ln(x_n - x_0) \end{bmatrix}$$

(3-63)

The optimized result obtained from equation (3-63) includes the damping coefficient α, which will be compared to the theoretical result k_{imag}. To extract the experimental damping coefficient, several signals at different receiving locations are recorded. The maximum amplitude of each modes(maximum value of the packet envelope), the time of arrival (TOA) and the distance between the source and receiver are recorded. The slope of the curve in the ToA-distance plot is considered as the group velocity of the mode at this frequency. Since different modes are hard to be separated when the source and receivers are too close to each other, data with only constant group velocity is selected.

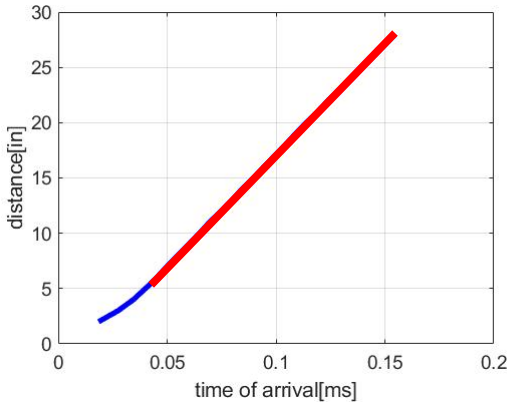

Figure 3-22 Selected data that forms constant group velocity

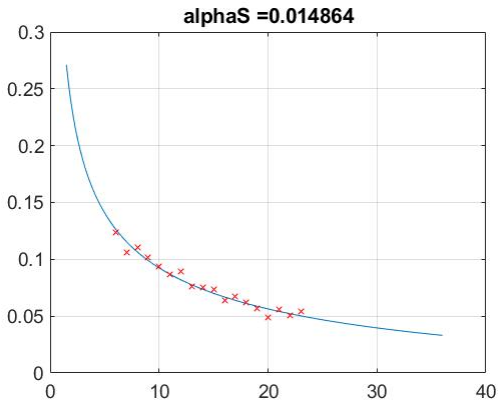

Figure 3-23 Sample of obtaining the α value from the optimization problem, blue curve is the optimized (3-62) and the red dots are the experimental amplitudes

After obtaining the damping coefficients α for $A0$ and $S0$ modes at different frequencies, the results are compared to the theoretical model. Both the group velocity (related to the real wave number) and the damping coefficient (imaginary wave number) are included in the comparison in the result.

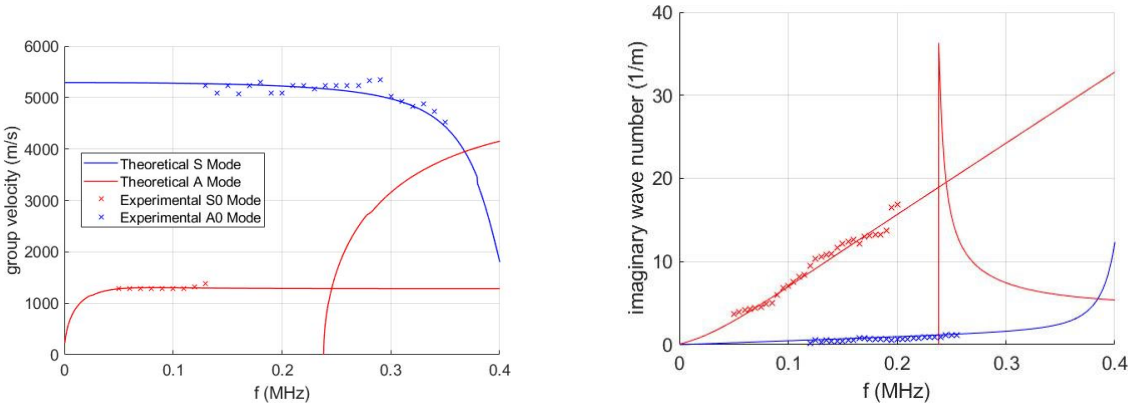

Figure 3-24 Comparison between the theoretical value and the experimental value for a)group velocity and b)imaginary wave number

By adjusting the p factor mentioned in the previous chapter, the theoretical values can match the experimental value when $p = 0.035$. From Figure 3-24, it can be seen that $A0$ mode damping

coefficient increases linearly with increasing frequency, and $S0$ mode has way less damping coefficient compared to $A0$ mode, which means they are less likely be affected in long range detection when the frequency increases. For higher modes, the damping coefficient is large when it is close to the cut-off frequencies.

Chapter 4 Experiments on Waves Propagating in Honeycomb Sandwich Structures

NDE using guided wave has several advantages. Compared to other NDE method, using guided waves can greatly reduce the cost and the amount of time required for obtaining data. Research has been done to determine the damage index to detect a crack in an aluminum plate [34], to detect facesheet damage in a honeycomb sandwich panel [35], to monitor the cure process [36], to determine the damage size in a plate [37] and to locate the barely visible impact damage (BVID) in a composite plate [38]. Other researches have focused on signal processing in order to obtain better signal to noise ratio [39, 40]. In this chapter, an experiment is done to quantify the features of core-skin disbond in honeycomb sandwich structures and a new damage index is proposed to obtain a damage graph with better resolution. Besides, the feasibility of using non-contact transducers pair to detect damages in HSS is studied.

4.1 Experiments on the core-skin disbond in a honeycomb sandwich structure

4.1.1 Experimental setup

The honeycomb sandwich structure(HSS) specimens used in this study have face sheets of woven carbon fiber composites while the core is made of cylindrical aluminum hexagons with cell size of approximately 9 mm and cell wall thickness of 0.12 mm. The face sheets are 1.78 mm thick and the core is 12.7 mm thick. The excitation signals used in the experiments are 5-cycle Hann windowed sine waves and a chirp signal covering the frequency range of 20 kHz to 220 kHz. To generate the signals, an NI PXI-5402 function generator is used. The actuators and receivers used in the experiment are broadband transducers, B225, from Digital Wave

Corporation. An Agilent 54624A oscilloscope is used for recording and transmitting the signals. The recording interval of time is 0.4 ms with a sampling frequency of 5 MHz. As shown in Figure 4-2, the transducers are mounted onto the surface of the specimen via C-clamps to guarantee uniform force on the contact surfaces. The disbonds at the top and bottom interfaces are created in 1-cm increments with ultrasound recording between the disbond extensions. Responses at different frequencies are also compared by extracting the narrowband signals from the broadband chirp signal.

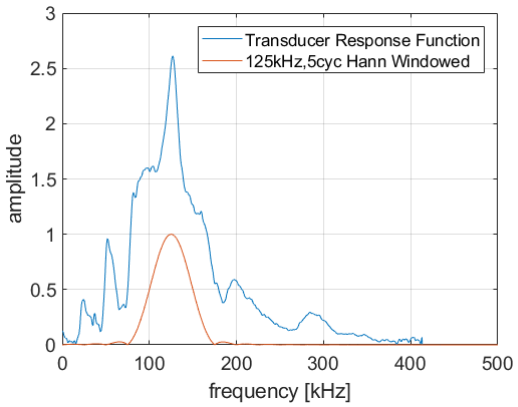

Figure 4-1 Spectra from a face-to-face experiment and Hann windowed signal used in the experiments

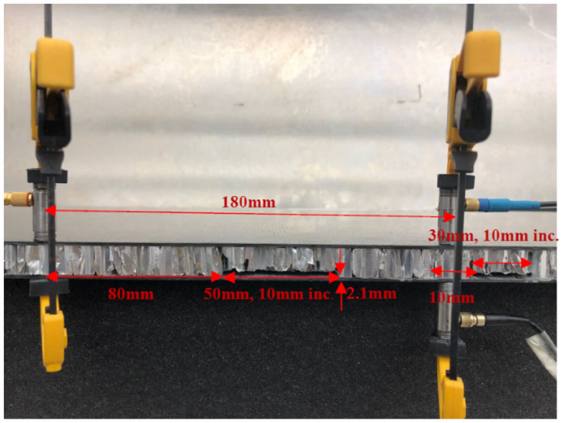

Figure 4-2 Experimental setup for a disbond at the bottom interface

4.1.2 Response of honeycomb sandwich structure

Before extracting the damage feature, the Lamb waves' modal response was studied at different excitation frequencies extracted from a broadband signal. The narrowband signal extracted from the broadband signal is affected by the transducer response. As shown Figure 4-1, the face-to-face transducer response has a peak at around 125 kHz and therefore this frequency is chosen for further analysis.

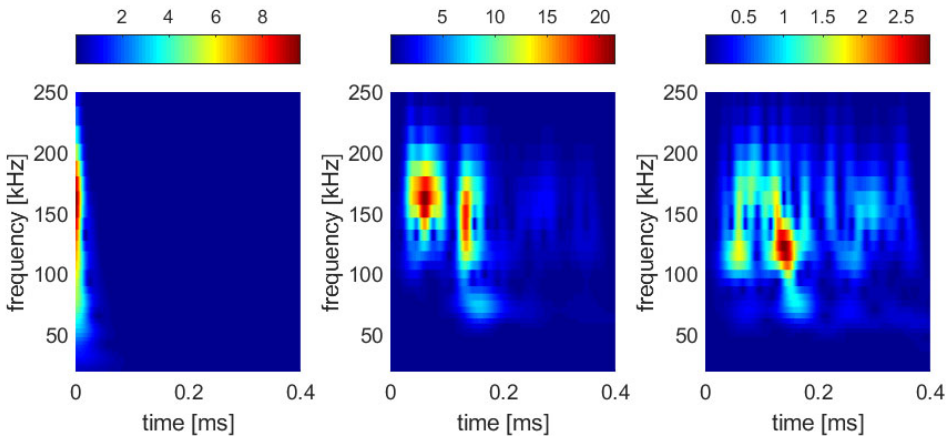

Figure 4-3 Wavelet transform of the signals for a)broadband source after pulse compression and b)top surface response c)bottom surface response

Pulse compression [41] is widely used in radar signal processing to improve time-domain resolution of broadband signals. By applying pulse compression to the signals and applying the wavelet transform, the time-frequency domain results for the signals at the top and bottom surfaces are shown in Figure 4-3. The source (auto-correlation of the chirp signal) is a broadband signal from 20 kHz to 220 kHz. The input signal has a maximum response at about 160 kHz while the output signals for the top and bottom surfaces show complicated patterns at different excitation frequencies. As can be seen in Figure 3b), there are two modes for the top surface. The first mode is represented by a wider vertical ellipse and the second mode by the narrower vertical

ellipse. This indicates that the first mode has a longer time duration and a higher velocity (shorter in time of arrival) with a maximum response at around 160 kHz. The second mode has a shorter time duration and a lower velocity (later time of arrival). However, the waves are dispersive, and coda waves caused by the natural vibration of the specimen appear at the bottom surface. This indicates that the time of arrival of the bottom surface modes has a frequency-dependent change due to the core structure.

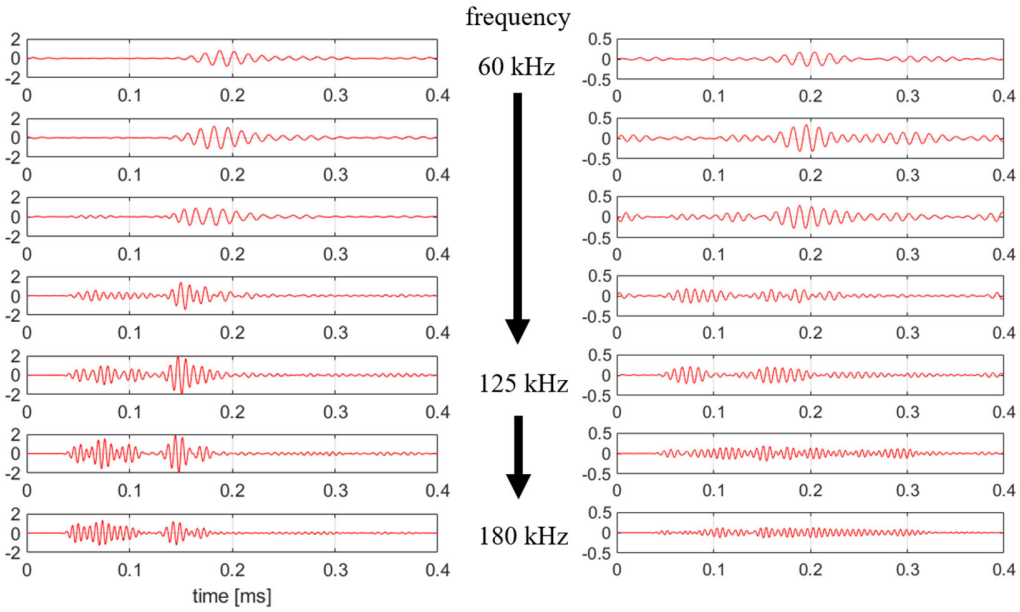

Figure 4-4 Recorded response on the top surface at different frequencies

In Figure 4-4, comparing the signals for different frequencies, there is more distinct mode separation at 125kHz, and this frequency is more convenient for monitoring the two different packets independently when the disbond is introduced.

4.1.3 Damage feature extraction

Disbonds are introduced outside the path of the directly waves between the source and the receiver while the sensors are placed on the reflection side behind the disbonds. Any damage

features observed from these three sets of data are attributed to the reflected waves from the disbond.

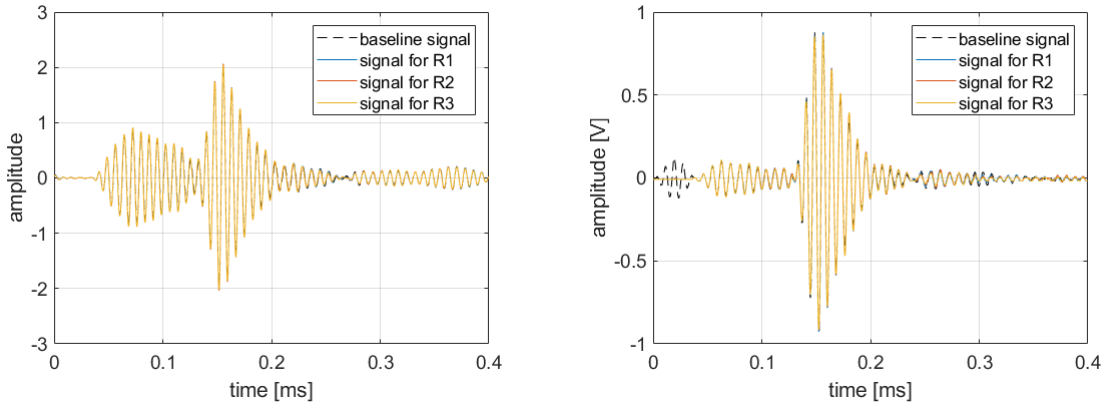

Figure 4-5 Damage features from reflected signals for a)top interface disbond and b)bottom interface disbond

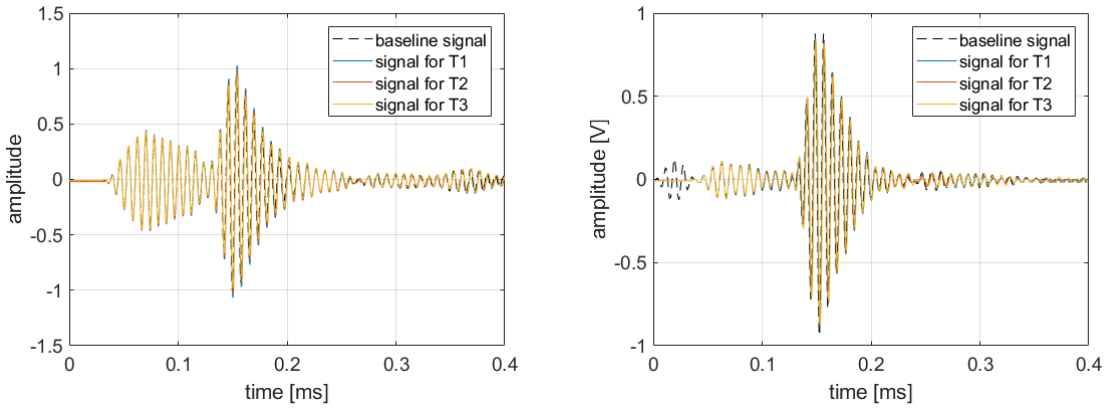

Figure 4-6 Damage features from transmitted signals for a)top interface disbond and b)bottom interface disbond

Figure 4-5 a) and b) show that the signal is insensitive to disbonds outside the propagation path, making it difficult to detect disbonds using the reflected waves. Figure 4-6 shows that the second packet is sensitive to both top and bottom interface disbonds. The damage features include changes in both phase and amplitude of the signals. The velocity of the mode is calculated from the experiment to be 1538 m/s, with an error of less than 6.5%. The calculations show that the

materials of the specimen are highly heterogeneous and anisotropic, especially under high frequency excitations. In order to address this issue, a time window is constructed by first finding the main packet that has the highest amplitude. Then, the time of arrival for this packet is obtained from the time of the envelope's peak. Finally, the window width is 95% of the excitation burst period, which is expressed in mathematical form:

$$w = [TOA - \frac{0.95k}{2f_c}, TOA + \frac{0.95k}{2f_c}] \tag{4-1}$$

where ToA is the time of arrival, fc is the central frequency of the source and k is the number of cycles. With this window, the packet containing the damage features can be selected as shown in Figure 4-7.

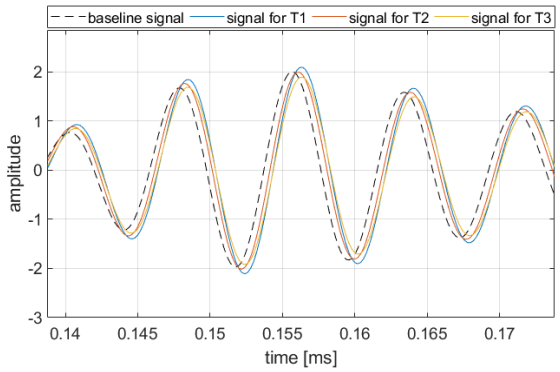

Figure 4-7 Selected signals containing damage features for different damage size, T1, T2 and T3 are 1, 2 and 3 cm respectively

The phase of the signal changes progressively due to an increase in the disbond size. Since signal amplitude is affected by many other factors such as electrical impedance, acoustic coupling and mechanical pressure, it is not an ideal damage index. To quantify the phase change of the signal, the delay in the cross-correlation of two signals is used. The damage index (DI) is defined as:

$$DI = \left(\frac{\tau_i}{\tau_{max}}\right)^{\alpha}$$

$$\tau_i = \left|index(\max\left(xcorr\left(\bar{f}_{damage}(w), \bar{f}_{baseline}(w)\right)\right))\right|$$

(4-2)

where w is the selected time window, $\bar{f}$ is the time domain signal, τ_{max} is the measured peak delay from the experiment, which is set to be 5 here and α is the coefficient to increase the sensitivity of the damage index. With this improved DI, the existence of a disbond between the detection transducer pair can be detected.

4.1.4 NDE using damage index

Once the DI is determined, an imaging method is applied. Reflection-based methods such as the delay-and-sum method or time reversal method, are not applicable for HSS because of the weak reflections. As pointed out in the introduction, to image the damage using transmitted signals, the RAPID method is used. The method uses a spatial function $F_\beta(x, y)$ to indicate the influence of the direct signal path:

$$F_\beta(x,y) = \begin{cases} \dfrac{\beta - r_\alpha(x,y)}{\beta - 1} & r_\alpha(x,y) < \beta \\ 0 & r_\alpha(x,y) \geq \beta \end{cases}$$

$$r_\alpha(x,y) = \frac{r_a(x,y) + r_s(x,y)}{\mathrm{d}}$$

(4-3)

where r_α is the distance between the sensor and the actuator, $r_a(x, y)$ is the distance between the imaging point and the actuator, and $r_s(x, y)$ is the distance between the imaging point and the sensor. The function describes the probability of damage in the path and β is the constant that decide the size of the influence region. When $r_\alpha(x, y)$ is large (far from the path), the $F_\beta(x, y)$ is

close to zero, indicating a small influence. When $r_\alpha(x,y)$ is close to one (on the path), $F_\beta(x,y)$ is close to one.

However, the sensor point is normally a crossing point of several paths, which introduces a statistical possibility of concentration. To avoid this, another spatial function $F_\gamma(x,y)$ is introduced to improve the current RAPID implementation:

$$F_\gamma(x,y) = \begin{cases} \dfrac{\min\left(1, \left(1-\left(r_a - \frac{r_\alpha}{2}\right)^\gamma\right)\right)\min\left(1, \left(1-\left(r_s - \frac{r_\alpha}{2}\right)^\gamma\right)\right)}{\left(\frac{r_\alpha}{2}\right)^{2\gamma}} & r_a < \dfrac{r_\alpha}{2} \ or \ r_s < \dfrac{r_\alpha}{2} \\ 1 & otherwise \end{cases} \tag{4-4}$$

Graphical representations of $F_\beta(x,y)$ and $F_\gamma(x,y)$ are presented in Figure 4-8.

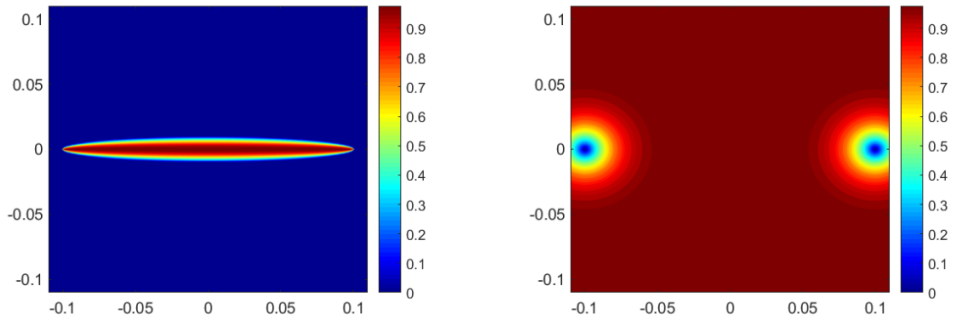

Figure 4-8 Plot for $F_\beta(x,y)$ and $F_\gamma(x,y)$ when $\beta = 1.005$ and $\gamma = 6$

Using these two spatial distribution functions, the path probability, P_α, and the final probability, $P(x,y)$, are defined as:

$$P_\alpha(x,y) = DI_\alpha F_\beta(x,y) F_\gamma(x,y)$$

and

$$P(x,y) = P_i(x,y) \cup P_j\,(x,y) = P_i + P_j - P_i P_j \tag{4-5}$$

$P(x,y)$ can be represented as a contour plot in the spatial coordinate system for the inspect region as will be shown later.

4.1.5 Damage detection demonstration on a aircraft structure

This method is applied to a section of an Airbus 330 elevator with a hexagonal sensor array using PZT patches. The elevator is made of a woven CFRP skin and a nomex core of thickness similar to that of the aluminum core used in the experiment. The sample and the sensor array are shown in Figure 4-9.

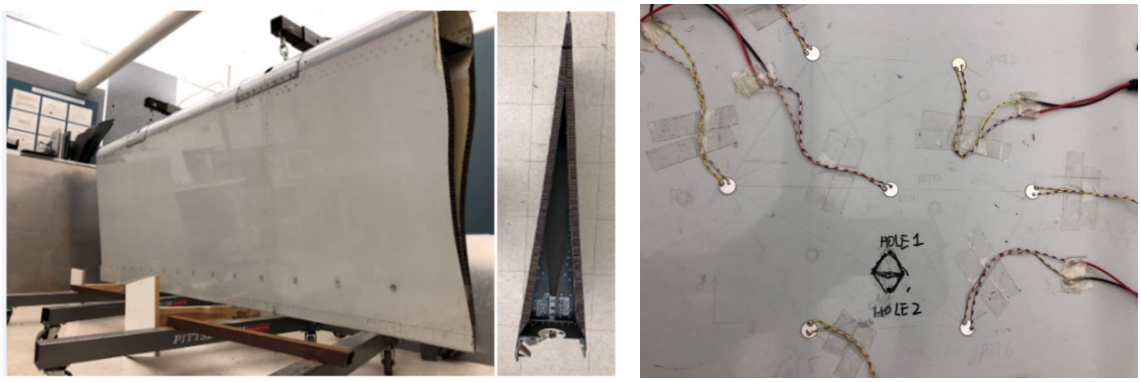

Figure 4-9 HSS from an elevator of Airbus 330, hexagonal array of PZT patches and introduced damage

The damage is introduced by first drilling a small hole and then using an L-shape tool to produce a disbond at the core-skin interface around the hole. The area of the disbond is about 2 cm^2, on the crossing point of two paths. Baseline signals are taken after the hole is drilled and damage signals are taken after the core has been damaged further.

After applying the wavelet transform, a packet with a peak at around 110 kHz is obtained as shown in Figure 10. The coda waves are present when the frequency is close to or higher than 110 kHz. Low-frequency components are present when the frequency is lower than 60 kHz.

Signals for the nomex core shows similarities to the aluminum core in the time-frequency domain. It is likely that the signal packets are due to wave propagation in a cellular structure and are relatively independent of the core material.

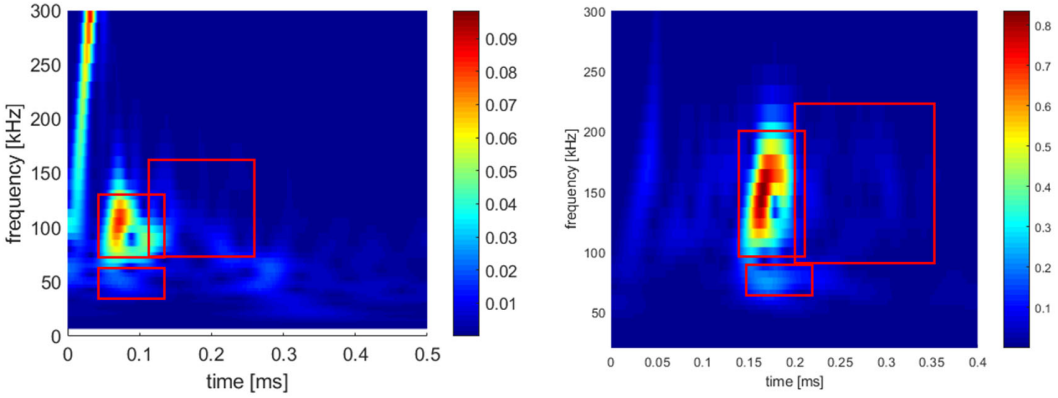

Figure 4-10 Comparison of the captured signals for a)nomex core and b)aluminum core

Traditional RAPID method uses the correlation coefficient between the baseline and damaged signal as a DI for imaging and considers the changes in signal. However, the Lamb wave scattering due to disbond would also introduce many small wave packets that cannot be filtered by the time window and would cause inaccurate damage location prediction. The DI proposed in this paper contains only the desired features and therefore, increases the accuracy.

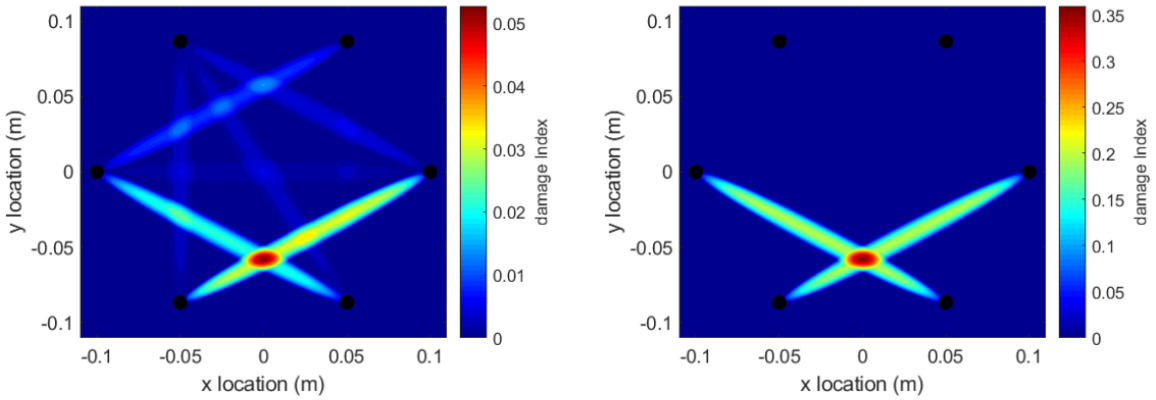

Figure 4-11 Damage index plot for a)correlation coefficient and b)proposed DI

4.2 Feasibility study of non-contact nondestructive evaluation of a honeycomb sandwich structure

Using guided ultrasonic waves for damage detection relies on the fact that any anomalies in the waves' path between actuator and sensor result in alterations that can be measured at the sensor. The evaluation and comparison of all measure wave paths is implemented via damage indices. The DI used in this paper is based on the energy of the signal. To this end, the relevant portion of the signal f is selected ($t_k \leq t \leq t_{k+N}$) and transformed into frequency domain using

$$\boldsymbol{F}(\omega) = \sum_{k=1}^{N} f_k e^{i\omega k t}$$

Taking the square of the Euclidean norm of the array $\boldsymbol{F}$, i.e.

$$E = \boldsymbol{F}^* \cdot \boldsymbol{F} \tag{4-6}$$

for both the baseline signal (denoted by $_{UD}$) and the signal recorded on the damaged specimen (denoted by $_{D}$), the DI is determined by

$$DI = \left|1 - \frac{E_D}{E_{UD}}\right| \tag{4-7}$$

If there is no damage present in the ``damaged'' wave path, the norm will be equal to that of the baseline, i.e. $E_D = E_{UD}$, and the DI will be zero. Hence, any non-zero DI indicates an anomaly, such as a delamination or disbond. The DI is calculated and related to the (x, y) coordinates. Then a 2D interpolation algorithm is applied to generate a heat map for visualizing the damages.

4.2.1 Experimental setup

Two specimens are investigated in this work: 1) a sandwich panel with an aluminum honeycomb core and CFRP face sheets and 2) a CFRP plate. The CFRP plate is $17.32\ in\ \times 17.32\ in$ and has a stacking sequence of $[0, \pm 45, 90, 90, \mp 45, 0]_s$, leading to a total thickness of $0.106\ in$. The HSP, is $355.98\ in\ \times 355.98\ in$, with a core thickness of $0.5\ in$ and a skin thickness of $0.07\ in$, thus leading to total thickness of $0.64\ in$. The geometrical material properties for the panel and plate are shown in Table 4-1. Effective material properties are determined with the use of classical lamination and mixture theories [28].

Table 4-1 Geometry and effective material parameters for the skin and core of the HSP and a CFRP plate with quasi-isotropic stacking sequence

	$L\ [in]$	$W\ [in]$	$2H\ [in]$	$E_{11}\ [Msi]$	$E_{33}\ [Msi]$	ν_{12}	ν_{13}	$G_{13}\ [Msi]$	$\rho\ [lb/ft^3]$
HSP-Skin	35.98	35.98	0.07	5.63	1.4	0.314	0.324	0.43	79.66
HSP-Core	35.98	35.98	0.5	0.0004	0.43	0.999	0.33	0.06	7.12
CFRP	17.32	17.32	0.106	6.44	1.96	0.29	0.33	0.67	96.33

The induced damage in the HSP is a $2\ in\ \times 2\ in$ disbond between the top skin and the core, while the damage for the woven, quasi-isotropic CFRP plate consists of a $2\ in\ \times 2\ in$ delamination. Both are at the center of the plates.

The data generation and acquisition are performed with an NI PXI-5402 function generator with a sampling frequency of 100 MHz and Agilent 54624A scope, respectively.

The utilized transducers and sensors are broadband contact transducers (CT, Digitalwave B225), air-coupled transducers (ACT, Sonotec CF200) and a laser Doppler vibrometer (LDV, Fiber Interferometer Polytec OFV 512 and controller OFV 3001).

The plates are actuated with a 200kHz 10cycles Hann window signal, which corresponds to the excitation frequency of the ACT. The data is recorded with a 10 MHz sampling frequency in 0.2 ms to avoid boundary reflection. The sensing velocity range is 5mm/s/V for LDV. A 20kHz to 500kHz bandpass Bessel filter was applied to denoise the raw acquired signals before they were used to calculate the damage index.

In order to study the detectability of defects in HSP with non-contact actuators and sensors, the ACT excitability was first determined. To find the optimal angle, the HSP was actuated at different angles ranging from 9° to 18° and the signal was sensed with the LDV located 2 inches from the ACT, as shown in Figure 4-12.

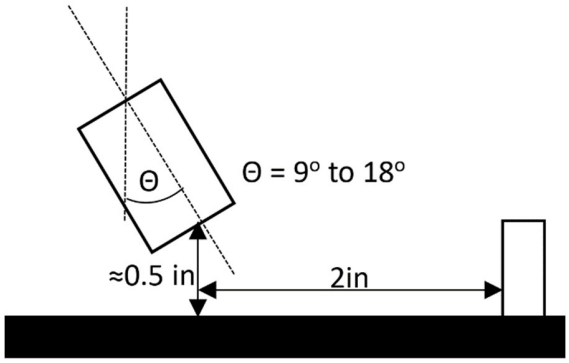

Figure 4-12 ACT optimal angle

The optimal angle for ACT actuating is obtained by calculating the energy of the signal and the maximum amplitude of the signal.

The scanning area in HSP and CFRP experiment is limited to 4 in × 6 in in a rectangular array. Figure 3 shows the position of the actuator(red dots), the receiver(black dots), and the damaged area. For accurate placement of the contact transducers, a Plexiglas template is used. To improve the energy transmission, Sonics ultrasonic coupling gel was applied between the transducers and the composite plate. In addition, an auto-control system is applied for positioning the ACT, showed in Figure 4-14.

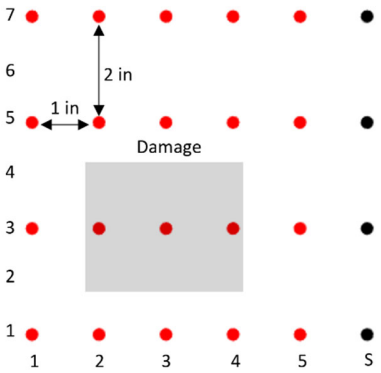

Figure 4-13 Scanned area with actuator position(red dots) and receiver position(black dots)

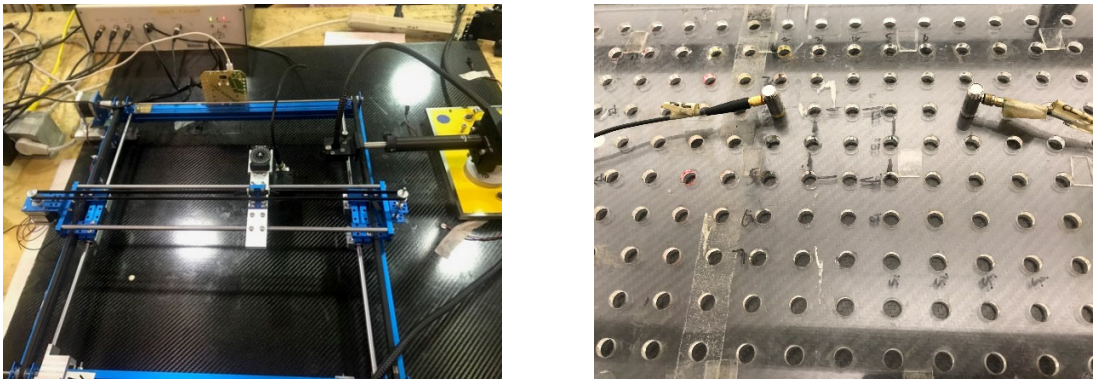

Figure 4-14 Experimental setup for scanning

4.2.2 Results and conclusion

The results are shown in Figure 4-15. Both results show a peak at 12° to 13°. With the sound speed in air 334 m/s and the Snells law, the phase velocity in HSS is computed to be around 1480 to 1600 m/s.

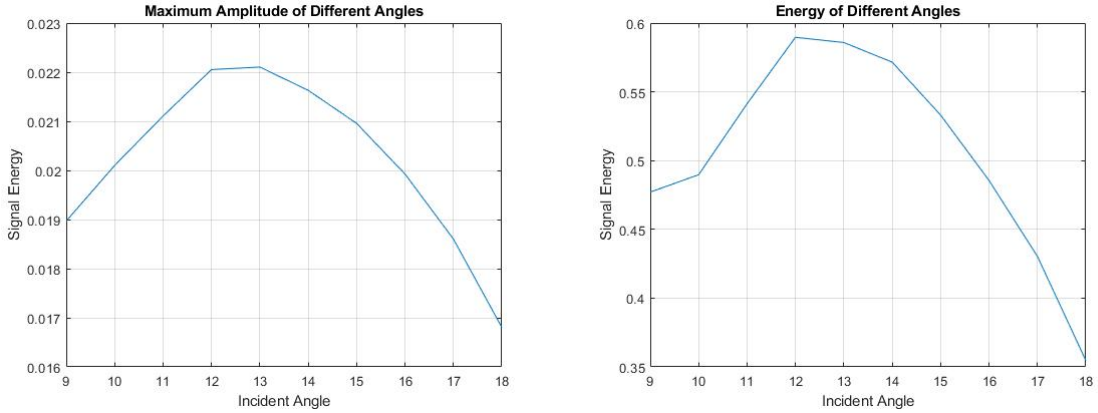

Figure 4-15 Excitability of different angles in terms of a)maximum amplitude b)signal energy

The results of scanning the woven composite plate show that the energy based damage index is capable to detect delamination and the signal energy decreases significantly compared to the healthy path after the wave front passes the damage, as shown in Figure 4-16.

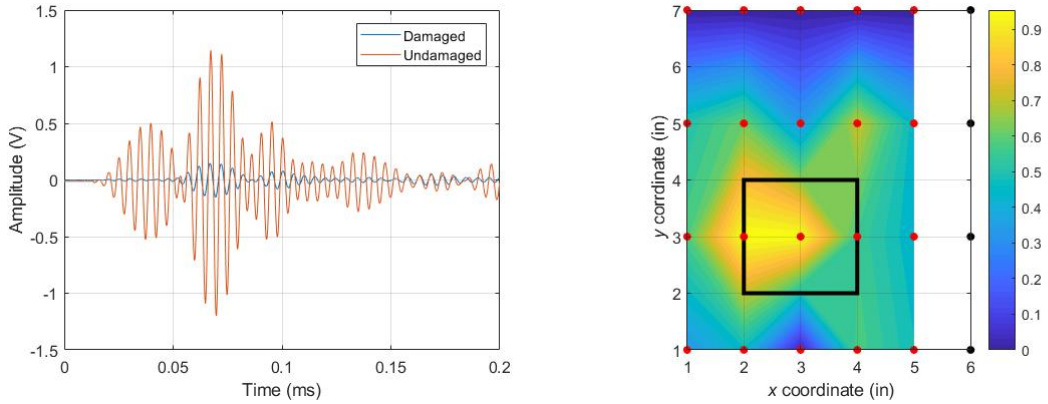

Figure 4-16 Results for CT to CT damage detection in CFRP plate a)raw signals from pristine and damaged paths and b)heat map of DI

In this case, the path that is furthest from the damaged area is chosen to be the healthy path, with 7 inches in y coordinate. It should be noticed that the damage index is very sensitive to the choice of healthy path, or in another word, baseline signal.

The HSP sample with an induced disbond was studied by a CT to CT scanning sensor array, the results are shown in Figure 4-17.

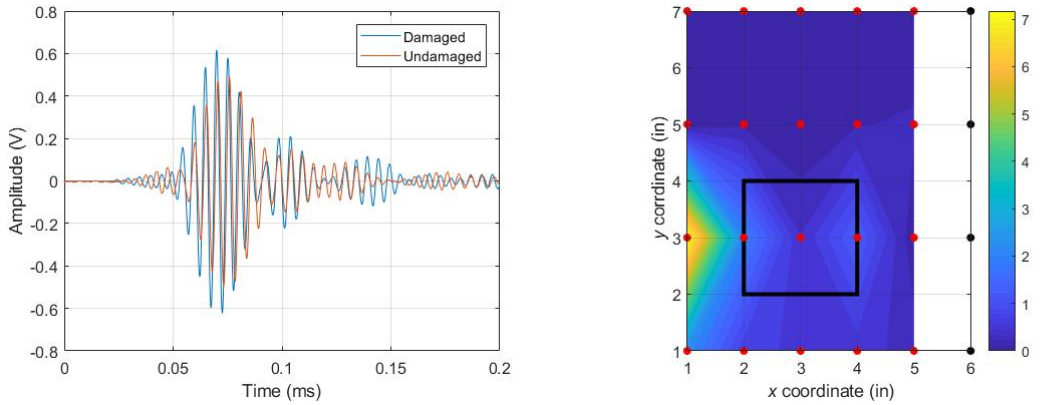

Figure 4-17 Results for CT to CT damage detection in HSP

The results show that the HSP for 200 kHz frequency cannot use the time windowed energy as a DI. One of the reason may be that lamb wave in HSP contains a lot more information than CFRP. Those information may come from the geometry and mode complexity of the core. For 200 kHz frequency, the honeycomb geometry may not be considered as a homogeneous anisotropic material. Therefore, to simplify the geometry effect, a lower frequency is suggested for energy based DI damage detection. The second reason may be the choice of healthy path. As mentioned above, the energy based DI is very sensitive to the baseline signal. CTs are less robust to disturbance from changing coupling every time. Using CTs for NDE with any with-baseline DI can be complicated. Therefore, in this paper, the feasibility for using non-contact transducers on HSP detection are studied.

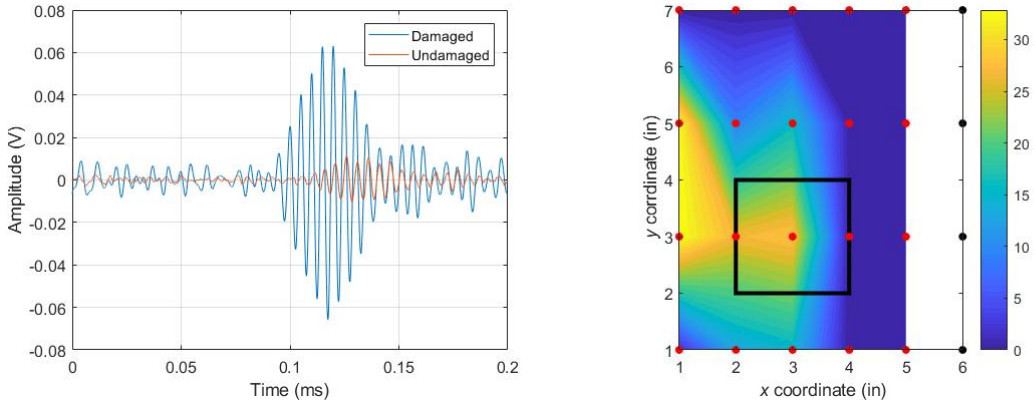

Figure 4-18 Results for ACT to LDV damage detection in HSS in a)raw signals from pristine and damaged paths and b)heat map of DI

The results for ACT are shown in Figure 4-18. The energy-based DI works for the HSP. The healthy path has smaller amplitude than the damaged path. However, the results are a lot noisy when the distance from source and sensors are more than 3 inches.

In conclusion, the results have shown that the DI is an effective indicator of delamination in composite plates with contact transducers. However, the results for detection of disbond in HSP using contact transducers, with a excitation frequency 200kHz, are inconclusive. A possible explanation for these results can be the lack of knowledge of the propagation mechanism for lamb waves in HSP. Finally, one alternative to improve the detection of disbond in HSP could be using non-contact transducers in a smaller detection area. Experiment using ACT and LDV has indicated that within 3 inches, disbond can be detected in HSP. The results showed an alternative scanning method using lamb wave for HSP without contact transducers, and with more than 10 times efficient than C-scan.

Chapter 5 Concluding Remarks and Future Work

5.1 Concluding remarks

In this dissertation, an improved theory is provided to solve the dispersion equations for large values of the frequency-thickness product is developed. With the tool, the dispersion curves and the response in high frequency domain are studied. The solution at one point is compared to FEM simulation at the same point. The theory of calculating Lamb wave mode shapes and theory of calculating Lamb waves in layered media are improved. These theories are used to solve several problems including studying the Lamb wave group velocity changes due to changes in the HSS core material properties. In addition, a Lamb wave damping model introduced earlier for composite structures was applied to honeycomb structures and damping factor was determined experimentally. An improved method for using damage indices in detecting core-skin disbond in HSS is developed based on several experiments. And the feasibility study of non-contact NDE in HSS is carried out experimentally.

In Chapter 2, for a 2-D plane strain Lamb wave problem, a new method is developed for finding the real roots of the dispersion equations efficiently. The tool considered a polar local domain with a new root-judging method, which provides a better convergence to the solution. With this tool, a wider range of dispersion curves can be studied. An approximate explicit form of dispersion curves when the frequency-thickness product is high enough is provided. The response of an aluminum plate under high frequency excitation is studied and compared with FEM simulation. Results show that with high frequency excitation, instead of studying the effect of a single mode, studying the total effect of certain region of all the modes provides a better physical meaning.

In Chapter 3, based on the traditional global matrix theory, a matrix form solution of the wave equations with removing the singularities is provided. A new method to obtain mode shapes based on singular value decomposition is proposed. New indices to quantify the quality of the dispersion data obtained by numerical tools are provided. A new study is conducted to explore how changes in the core material properties change the dispersion curves of a sandwich structure. The results show that different core properties dominate different part of the dispersion curves, which potentially can be a way for material characterizing. Finally, an experiment is conducted to validate the Q-factor based damping model and the corresponding "p" value is measured in experiment.

In Chapter 4, several experiments related to damage detection in honeycomb sandwich structures are conducted. First, an experiment is set up by introducing delaminations in HSS and compare the signals in the damaged and undamaged specimens. The results show that the transmitted signals are sensitive to the delamination at certain frequencies, while the reflection signals are not sensitive. Based on this fact, a new damage index is introduced to improve the damage image resolution. The same damage index is used on a sample HSS of an Airbus 330 and it shows result that the method is capable of estimating the damage location. In another experiment, the feasibility of using air-coupled transducers to detect the damage in HSS is studied. The result shows that although the air-coupled transducers have relatively low signal-to-noise ratio, it can potentially be introduced into NDE of HSS.

5.2 Future work

For the high frequency response, to separate different packet in the time domain, the cluster effect needs to be further studied. In the future, the searcher can be combined with global-local method in order to obtain the defect response.

The HSS is a very complicated structure. In this thesis, the core material is homogenized to simplify the study. To fully study the waves' behaviors in HSS, the discretized model needs to be considered. It is found in experiment that when the disbond is introduced, the waveform will not change a lot, which is difficult to be explained by the homogenized model. One of the possible explanations is that the honeycomb core plays a role that only absorbing energy for certain modes. More theoretical modeling and experiments need to be done on providing and validating the model. Besides, the thesis employed only 2D models. Certain aspects of this work can be improved through the use of 3D models.

References

[1] I. Viktorov, Rayleigh and Lamb Waves, Physical Theory and Applications, US: Springer, 1967.

[2] L. Nagy *et al.*, "Nondestructive Evaluation of adhesive joints by guided waves," *Applied Physics,* vol. 66, pp. 4658-4663, 1989.

[3] A. Mal, Z. Chang, "Scattering of Lamb waves from a rivet hole with edge cracks," *Mechanics of Materials,* vol. 31, pp. 197-204, 1999.

[4] X. Yu *et al.*, "Anisotropic effects on ultrasonic guided waves propagation in composite bends," *Ultrasonics,* vol. 72, pp. 95-105, 2016.

[5] S. Yashiro, J. Takatsubo and N. Toyama, "An NDE technique for composite structures using visualized Lamb-wave propagation," *Composites Science and Technology,* vol. 67, 2007.

[6] M. Michal, R. Mateusz, M. Adam, S. Tadeusz and U. Tadeusz, "PZT based tunable Interdigital Transducer for Lamb waves based NDT and SHM," *Mechanical Systems and Signal Processing,* vol. 76, pp. 71-83, 2015.

[7] F. Gao, J. Hua, L. Zeng and J. Lin, "Amplitude modified sparse imaging for damage detection in quasi-isotropic composite laminates using non-contact laser induced Lamb waves," *Ultrasonics,* vol. 93, pp. 122-129, 2019.

[8] D. W. Greve, P. Zheng and I. J. Oppenheim, "The transition from Lamb waves to longitudinal waves in plates," *Smart Materials and Structure,* vol. 17, no. 3, p. 035029, 2008.

[9] R. Hanna *et al.*, "A comparison of honeycomb-core and foam-core carbon-fibre/epoxy sandwich panels," *Composites,* vol. 21, no. 4, p. 325, 1990.

[10] H. R. Merriman, "Honeycomb Sandwich Panel Structure and Method of Making Same". United States Patent 2952579, 13 September 1960.

[11] V. K. Goyal, E. Koontz, "Proof Test Methodology for Reducing the Risk of Unvented Honeycomb Core Failures in Aerospace Structures," in *AIAA*, Kissimmee, 2018.

[12] L. Aktay *et al.*, "Numerical modelling of honeycomb core crush behaviour," *ScienceDirect,*

vol. 75, pp. 2616-2630, 2008.

[13] A. Mal, C. Schaal, "Core-Skin Disbond Detection in a Composite Sandwich Panel Using Guided Ultrasonic Waves," *Nondestructive Evaluation, Diagnostics and Prognostics of Engineering Systems,* vol. 1, p. 1, 2018.

[14] D. K. Hsu, "Nondestructive Evaluation of Sandwich Structures: A Review of Some Inspection Techniques," *Sandwich Structures and Materials,* vol. 11, p. 275, 2009.

[15] J. C. J. W. e. Jin Zhang, "Nondestructive evaluation of glass fiber honeycomb sandwich panels using reflective terahertz imaging," *Sandwich Structures and Materials,* vol. 21, no. 4, pp. 1211-1223, 2019.

[16] P. V. R. Usamentiaga, "Non-destructive inspection of drilled holes in reinforced honeycomb sandwich panels using active thermography," *Infrared Physics and Technology,* vol. 55, pp. 491-498, 2012.

[17] Yunze, "Non-destructive testing of low-energy impact in CFRP laminates and interior defects in honeycomb sandwich using scanning pulse eddy current," *Composites: Part B,* vol. 59, pp. 196-203, 2015.

[18] C. H. a. e. Christina J. Naify, "Transmission loss of honeycomb sandwich structures with attached gas layers," *Applied Acoustics,* vol. 72, pp. 71-77, 2011.

[19] H. Baid, C. Schaal, H. Samajder, A. Mal, "Dispersion of Lamb Waves in a Honeycomb Composite Sandwich Panel," *Ultrasonics,* vol. 56, pp. 409-416, 2015.

[20] S. M. H. Hosseini, U. Gabbert, "Numerical Simulation of the Lamb Wave Propagation in Honeycomb Sandwich Panels: A parametric Study," *Composite Structures,* vol. 97, pp. 189-201, 2013.

[21] S. M. H. Hosseini, U. Gabbert, "Damage Localization in Plates Using Mode Conversion Characteristics of Ultrasonic Guided Waves," *Journal of Nondestructive Evaluation,* vol. 10, pp. 152-165, 2014.

[22] S. M. H. Hosseini, U. Gabbert, "Analysis of Guided Lamb Wave Propagation (GW) in Honeycomb Sandwich Panel," *Proceddings in Applied Mathematics and Mechanics.,* vol. 10, pp. 11-14, 2010.

[23] A. K. Mal and S. J. Singh, Deformation of Elastic Solid, Prentice Hall, 1991.

[24] A. H. Nayfeh, Wave Propagation in Layered Anisotropic Media, Amsterdam: Elsevier, 1995.

[25] K. Peddeti and S. Santhanam, "Dispersion curves for Lamb wave propagation in prestressed plates using a semi-analytical finite element analysis," *The Journal of the Acoustical Society of America,* pp. 829-840, 2018.

[26] T. Hayashi, W.-J. Song and J. L. Rose, "Guided wave dispersion curves for a bar with an arbitrary cross-section, a rod and rail example," *Ultrasonics,* vol. 41, pp. 175-183, 2003.

[27] B. R. Mace, "Finite element prediction of wave motion in structural waveguides," *The Journal of the Acoustical Society of America,* vol. 117, pp. 2835-2843, 2005.

[28] C. Schaal, S. Bischoff and L. Gaul, "Analysis of wave propagation in periodic 3D waveguides," *Mechanical Systems and Signal Processing,* vol. 40, pp. 691-700, 2013.

[29] M. J. S. Lowe, "Matrix Techniques for Modeling Ultrasonic Waves in Multilayered Media," *Transactions on Ultrasonics, Ferroelectrics, and Frequency Control,* vol. 42, no. 4, pp. 525-542, 1995.

[30] H. Lamb, "On Waves in an Elastic Plate," *proceddings of the Royal Society A, Math. Phys. and Engi. Science,* pp. 114-128, 1917.

[31] W. T. Thomson, "Transmission of Elastic Waves Through a Startified Solid Medium," *Journal of Applied Physics,* vol. 22, pp. 89-93, 1950.

[32] N. A. Haskel, "The Dispersion of Surface Waves on Multilayered Media," *Bulletin of the Seismological Society of America,* vol. 43, pp. 17-34, 1953.

[33] J. W. Dunkin, "Computation of Modal Solutions in Layered Elastic Media," *Bulletin of the Seismological Society of America,* vol. 55, pp. 335-358, 1965.

[34] L. Knopoff, "A Matrix Method for Elastic Wave Problems," *Bulletin of the Seismological Society of America,* vol. 54, pp. 431-438, 1964.

[35] A. Mal, "Guided Waves in Layered Solids with Interface Zones," *International Journal of Engineering Science,* vol. 26, pp. 873-881, 1988.

[36] T. Kundu and A. K. Mal, "Elastic waves in a multilayered solid due to a dislocation source," *Wave Motion,* vol. 7, no. 5, pp. 459-471, 1985.

[37] E. J. Luco and R. J. Apsel, "On the Green's functions for a layered half-space. Part I," *Bulletin of the Seismological Society of America,* vol. 73, no. 4, pp. 909-929, 1983.

[38] A. Velichko and P. D. Wilcox, "Modeling the excitation of guided waves in generally

anisotropic multilayered media," *The Journal of the Acoustical Society of America,* vol. 60, p. 121, 2009.

[39] J. L. Rose, Ultrasonic Guided Waves in Solid Media, New York: Cambridge University Press, 2014.

[40] L. Wang and F. G. Yuan, "Group velocity and characteristic wave curves of Lamb waves in composites: Modeling and experiments," *Composites Science and Technology,* vol. 67, no. 7-8, pp. 1370-1384, 2007.

[41] Z. A. B. Ahmad, J. M. Vivar-Perez and U. Gabbert, "Semi-analytical finite element method for modeling of lamb wave propagation," *CEAS Aeronautical Journal,* vol. 4, pp. 21-33, 2013.

[42] A. Mal, "Guided Waves in Layered Solids with Interface Zones," *International Journal of Engineering Science,* vol. 26, no. 8, pp. 873-881, 1988.

[43] R. Jones, Mechanics of Composite Materials, Taylor, 1999.

[44] L. J. Gibson and M. F. Ashby, Cellular solids: structure and properties, Cambridge, UK: Cambridge university press, 1999.

[45] C. Schaal and A. Mal, "Dispersion of guided waves in composite laminates and sandwich panels," in *Proc. SPIE*, 2015.

[46] H. Baid, C. Schaal, H. Samajder and A. Mal, "Dispersion of Lamb waves in a honeycomb composite sandwich panel," *Ultrasonics,* vol. 56, pp. 409-416, 2015.

[47] A. Mal and S.-S. Lih, "Elastodynamic Response of Unidirectional Composite Laminate to Concentrated Surface Loads," *Journal of Applied Mechanics,* vol. 59, pp. 878-886, 1992.

[48] L. Knopoff, "Q," *Review of Geophysics,* vol. 2, pp. 625-660, 1964.

[49] A. K. Mal, C. Yin and Y. Bar-Cohen, "Analysis of acoustic pulses reflected from fiber-reinforced composite laminates," *Journal of Applied Mechanics,* vol. 59, no. 2, pp. 136-144, 1992.

[50] F. Ricci, E. Monaco, S. Tancredi, L. Lecce, S. Banerjee and A. K. Mal, "Detection in Composite Structures Theory and Experiments," *Nondestructive Testing of Materials and Structures,* pp. 577-582, 2013.

[51] S. M. H. Hosseini, S. Duczek and U. Gabbert, "Damage Localization in Plates Using Mode Conversion Characteristics of Ultrasonic Guided Waves," *Journal of Nondestructive*

Evaluation, pp. 152-165, 2014.

[52] S. Pavlopoulou, C. Soutis and W. J. Staszewski, "Cure Monitoring through time-frequency analysis of guided ultrasonic waves," *Plastics, Rubber and Composites,* vol. 41, no. 4-5, pp. 180-186, 2012.

[53] B. C. Lee and W. J. Staszewski, "Lamb wave propagation modelling for damage detection: II. Damage monitoring strategy," *Smart Material and Structures,* vol. 16, pp. 260-274, 2007.

[54] M. Dziendzikowski, A. Kurnyta, K. Dragan, S. Klysz and A. Leski, "In situ Barely Visible Impact Damage detection and localization for composite structures using surface mounted and embedded PZT transducers: A comparative study," *Mechanical Systems and Signal Processing,* vol. 78, pp. 91-106, 2015.

[55] P. Wilcox, "A Rapid Signal Processing Technique to Remove the Effect of Dispersion from Guided Wave Signals," *IEEE Transactions on Ultrasonics, Ferroelectrics, and Frequency Control,* vol. 50, no. 4, pp. 419-427, 2003.

[56] F. Gao, L. Zeng, J. Lin and Z. Luo, "Mode seperation in frequency-wavenumber domain through compressed sensing of far-field Lamb waves," *Measurement Science and Technology,* vol. 28, 2017.